Spectral fiber-photometry derives hemoglobin-absorption changes for accurate measurement of fluorescent sensors

Wei-Ting Zhang[1-3+], Tzu-Hao Harry Chao[1-3+], Yue Yang[1-4], Tzu-Wen Wang[1,2], Sung-Ho Lee[1-3], Esteban A. Oyarzabal[1-3], Jingheng Zhou[5], Randy Nonneman[1-3], Nicolas C. Pegard[6,7], Hongtu Zhu[2,4,8], Guohong Cui[5*], Yen-Yu Ian Shih[1-3,7*]

[1]Center for Animal MRI, University of North Carolina at Chapel Hill

[2]Biomedical Research Imaging Center, University of North Carolina at Chapel Hill

[3]Department of Neurology, University of North Carolina at Chapel Hill

[4]Department of Biostatistics, University of North Carolina at Chapel Hill

[5]In vivo Neurobiology Group, Neurobiology Laboratory, National Institute of Environmental Health Sciences, National Institutes of Health

[6]Department of Applied Physical Sciences, UNC Neuroscience Center, University of North Carolina at Chapel Hill

[7]Department of Biomedical Engineering, University of North Carolina at Chapel Hill

[8]Department of Computer Science, University of North Carolina at Chapel Hill

[+]These authors contributed equally

[*]Correspondence to Yen-Yu Ian Shih, Ph.D. (shihy@unc.edu) or Guohong Cui, M.D., Ph.D. (cuig@mail.nih.gov)

Abstract

Fiber-photometry is an emerging technique for recording fluorescent sensor activity in the brain. Here we demonstrate significant hemoglobin-absorption artifacts that may be misinterpreted as sensor activity changes. Because hemoglobin exists in nearly every location in the brain and its concentration varies over time, such artifacts could significantly impede the accuracy of photometry recording results. We present a novel use of spectral photometry technique and propose a computational method to quantify photon absorption effect from an activity-independent fluorescent protein, which can be used to derive oxy- and deoxy-hemoglobin concentration changes and correct target sensor activities across spectra. We further demonstrate the utility of this method for delineating brain regional differences in neurovascular transfer functions and shed light on the interpretation of hemodynamic-based neuroimaging data.

Main

Fiber-photometry relies on an implanted optical fiber to excite and detect fluorescence signals, and is best known for its ability to measure ensemble neuronal or neurochemical activity in small volumes of brain tissue in animal models. The simplicity and cost-effectiveness of the optical system make the technique highly accessible[1], and lightweight, miniature fiber optics make photometry compatible with a wide variety of experimental settings, such as freely moving behavioral assessment[1,2] or head-fixed brain-wide imaging[3,4] (**Fig. 1a**). Several genetically encoded fluorescent sensors of cellular activity and neurotransmitters have recently become widely available[5], expanding the range of applications for fiber-photometry. The tunable spectral specificity has further enabled new parallel sensing capabilities with wavelength multiplexing. Given its rapidly increasing usage in neuroscience[6–9], understanding the inherent confounding factors in fiber-photometry data is of paramount significance.

Perhaps the most notable confounder affecting fluorescence measurements is light absorption by hemoglobin (Hb) within blood vessels[10,11]. The Hb-absorption artifact should be present in most photometry data because the intervascular distance of capillaries is known to be < 60 μm in nearly every location in the brain[12] and commonly used photometry targeted volumes is 10^5–10^6 μm^3 [13]. This absorption occurs in two phases: along the excitation path, by absorbing photons that travel from the fiber tip to the targeted fluorescent proteins; and along the emission path, by absorbing photons emitted by the fluorescent proteins as they travel back towards the optical fiber (**Fig. 1b**). Both absorption effects add up and result in a substantial photon count reduction. Importantly, Hb-absorption is non-linear, wavelength-dependent, and varies as a function of dynamic oxy- and deoxy-hemoglobin (HbO and HbR) concentration changes *in vivo* (ΔC_{HbO} and ΔC_{HbR})[11,14] (**Extended Data Fig. 1**, derived from[11]), causing erroneous photometry reading. Further, because the power spectra of hemodynamic signals overlap significantly with most commonly used fluorescent sensors (**Extended Data Fig. 2**), hemoglobin related artifacts cannot be removed from fiber photometry data by notch filtering or regressing either cerebral blood flow or cerebral blood volume (CBV) signals. To the best of our knowledge, the influence of Hb-

absorption on fiber-photometry-derived fluorescent sensor activity has never been studied. The ability to quantify Hb concentration fluctuations in photometry data would not only enable more accurate fluorescent sensor activity measurements, but would also provide concurrent hemodynamic metrics, which is the foundation of several brain-mapping techniques including functional magnetic resonance imaging (fMRI)[15], intrinsic optics[16], and functional ultrasound[17].

In this study, we propose a novel use of spectrally resolved fiber-photometry platform and a computational method that can independently derive HbO and HbR concentration changes from static fluorescent reporter signals. We present the use of this technique to remove the Hb-absorption artifacts from calcium activity recording and demonstrate the added benefit to compute transfer function between neuronal and vascular activity which is crucial for interpreting hemodynamic-based neuroimaging data such as fMRI, functional ultrasound, and intrinsic optics.

Results

Theoretical Hb-absorption **effect on photometry recordings**

We solved the following equation using the generalized method of moments (GMM)[18] with spectrometer outputs, which provides quantifiable photon counts across spectra:

$$\frac{F(t,\lambda_{Em})}{F(t_0,\lambda_{Em})} = \mathrm{e}^{-[\Delta\mu_a(t,\lambda_{Ex})X(\lambda_{Ex})+\Delta\mu_a(t,\lambda_{Em})X(\lambda_{Em})]} \cdot \frac{C(t)}{C(t_0)} \tag{1}$$

where $\Delta\mu_a(t,\lambda_{Ex})$ and $\Delta\mu_a(t,\lambda_{Em})$ represent the absorption coefficient changes at excitation wavelength λ_{Ex} and emission wavelength λ_{Em} , respectively, at time point t as compared to a reference time point t_0. Both $\Delta\mu_a(t,\lambda_{Ex})$ and $\Delta\mu_a(t,\lambda_{Em})$ are affected by ΔC_{HbO} and ΔC_{HbR} (see Method Equation 16). $X(\lambda_{Ex})$ and $X(\lambda_{Em})$ represent the photon traveling pathlengths (see Methods for details) at the excitation and emission wavelengths, respectively. To solve equation (1), we first performed a Monte Carlo simulation using the pipeline shown in **Extended Data Fig. 3** to obtain $X(\lambda_{Ex})$ and $X(\lambda_{Em})$. We determined the average photon traveling pathlengths for emission wavelengths from 488 nm to 700 nm in the

simulated brain tissue from a total of 29 simulations (2-2.5 $\times 10^4$ photons each) in **Fig. 1c**, with detailed numbers tabulated in **Extended Data Table 1**. As an example, we illustrated spatial probability and luminance-distance profiles for the commonly used 488 nm excitation, 515 nm emission and 580 nm emission in **Extended Data Fig. 4a-c** (see also **Extended Video 1**). These results allowed calculating the simulated effects of Hb-absorption on fluorescence signal measurement, for which we observed significant nonlinear, wavelength-dependent effects (**Extended Data Fig. 4d**).

Ex vivo quantification of Hb-absorption effects on photometry recordings

We first performed *ex vivo* measurements and showed that adding 1 mL of fresh, venous mouse blood into a 10 mL mixture of Alexa 488 and 568 fluorescent dye solution significantly reduced both fluorescence signals measured by fiber-photometry (**Extended Data Fig. 5a**). Subsequently, we saturated the mixture with 100% oxygen to increase the HbO-HbR ratio and observed marked increases in the Alexa 568 signals but decreases in Alexa 488 signals (**Extended Data Fig. 5b**).

In vivo quantification of Hb-absorption effects on photometry recordings

We performed an *in vivo* experiment to measure the Hb-absorption of static fluorescence signals in fiber-photometry. We selected a commonly used fluorophore, enhanced yellow fluorescent protein (EYFP), whose fluorescence signal is activity-independent and has an emission spectrum peaking at 526 nm. We virally expressed EYFP using adeno-associated virus (AAV) in the primary somatosensory cortex (S1) of the forelimb region (S1FL) under the calmodulin kinase IIα (CaMKIIα) promoter and then implanted an optical fiber into this target area (**Fig. 1d,e**). On the day of photometry recording, we intravenously administered Rhodamine B, a long-circulating red fluorescent dye, to enable steady-state CBV measurements[19] (**Fig. 1f**) and cross validate our proposed method in calculating total Hb concentration changes. Of note, the resulting EYFP and Rhodamine B spectra overlapped significantly with the Hb-absorption spectra (see **Extended Data Fig. 2**), suggesting a significant impact of Hb-absorption on the

data from these fluorescence signals. Upon electrical stimulation of the contralateral forepaw (9 Hz, 3 mA, 0.5 ms pulse width for 10 s), we observed robust positive Rhodamine-derived CBV (rhoCBV) changes as expected (**Fig. 1g**). Intriguingly, the EYFP signal concurrently recorded from the same fiber showed robust negative changes, which indicated significant Hb-absorption of the EYFP signal *in vivo* (**Fig. 1h**). Using well-documented molar extinction coefficients (**Extended Data Fig. 1**), photon-traveling pathlengths derived from a Monte Carlo simulation (**Fig. 1c**), and spectral fiber-photometry datapoints across 502 – 544 nm wavelengths over time (see equation (17-21) in **Methods**), we derived $\Delta C_{HbO}(t)$ and $\Delta C_{HbR}(t)$ using GMM. Notably, this is possible because we have access to a range of spectral datapoints for every single time point and therefore could use numerous empirical data to solve two unknowns (ΔC_{HbO} and ΔC_{HbR}, see also **Extended Data Fig. 6** for the effect of input spectral datapoints). The derived concentration changes (**Fig. 1i, j**) were within physiological ranges and comparable to those reported in the literature[10], and the summation of the two (i.e., total Hb concentration changes, termed as $\Delta C_{HbT}(t)$) informs CBV changes[10] (**Fig. 1m**). The calculated $\Delta C_{HbT}(t)$ highly resembled the rhoCBV changes measured from a distinct and less-affected red spectrum (**Extended Data Fig. 7**). With $\Delta C_{HbO}(t)$ and $\Delta C_{HbR}(t)$ obtained, we then calculated $\Delta\mu_a(t,\lambda_{Ex})$ and $\Delta\mu_a(t,\lambda_{Em})$, and input these parameters into equation (1) to correct the rhoCBV changes (**Fig. 1k**) and EYFP signals (**Fig. 1l**). Indeed, **Fig. 1l** shows a flattened EYFP trace following the proposed correction, demonstrating the validity of our approach. Although the influence of Hb-absorption on EYFP signal varied by trials, our proposed method accurately corrected EYFP signals in all trials (**Fig. 1n**). Notably, despite the smaller influence on the rhoCBV signal measured from the red spectrum, the absorption effect remained statistically significant (**Fig. 1o**). In addition to the fluorescence signal changes induced by forepaw sensory stimulations, we also replicated these findings using a 5% CO_2 hypercapnic challenge paradigm and successfully restored the affected EYFP signal changes (**Extended Data Fig. 8**).

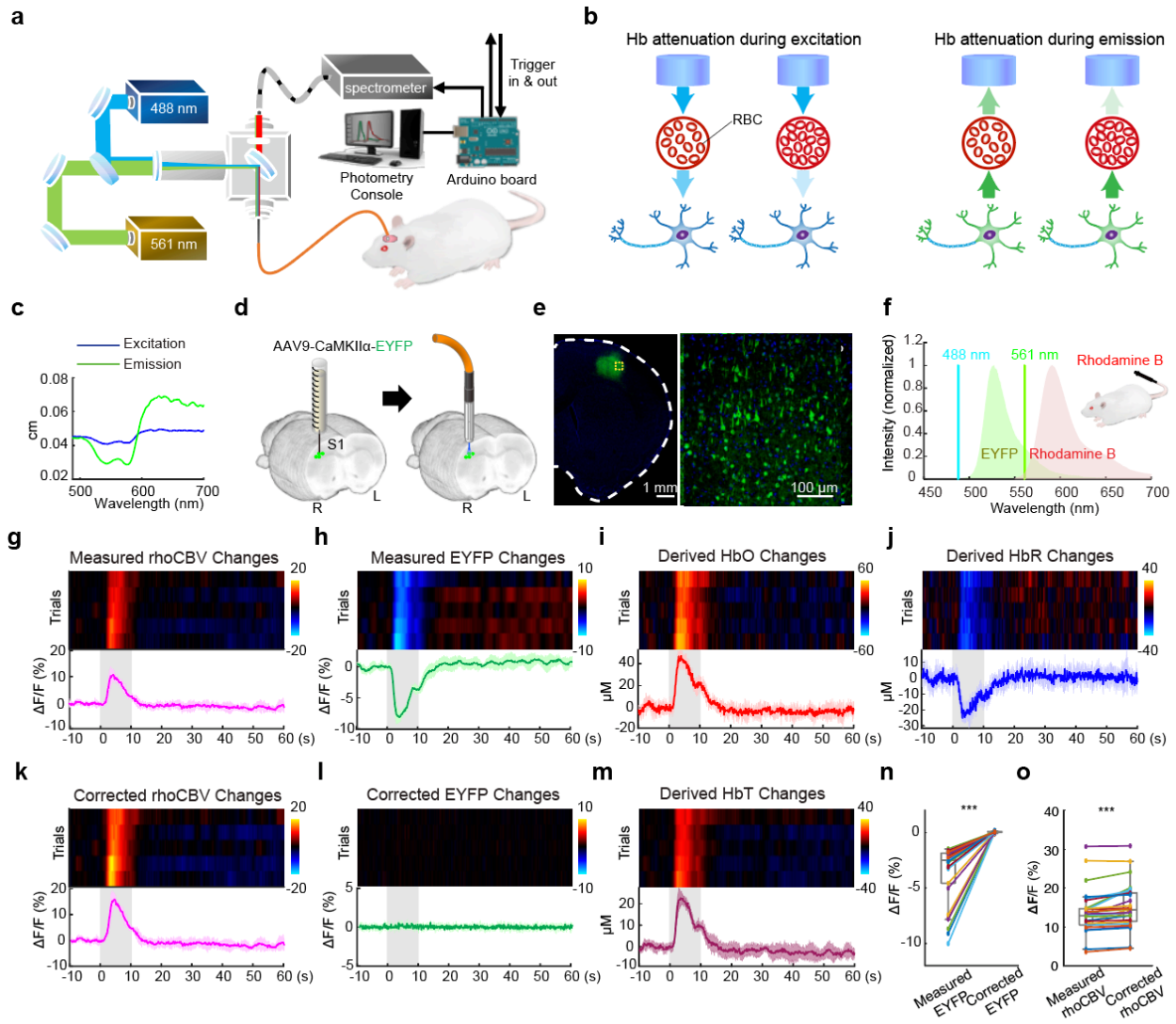

Fig. 1 *In vivo* quantification of Hb-absorption effects on fiber-photometry recordings. (**a**) Schematic illustration of a spectrally resolved fiber-photometry system used for recording fluorescence signals from rats. (**b**) Schematic illustration to show that Hb in red blood cells attenuates the excitation and emission photons emitted and collected by the optical fiber. (**c**) Simulated average excitation and emission photon traveling pathlengths across 488 – 700 nm emission wavelengths from the database of paired excitation/emission light paths. (**d**) Fiber-photometry measurement of EYFP signal in the S1 of the forelimb region. (**e**) Confocal images showing EYFP expression. (**f**) Simultaneous dual-spectral photometry recording of EYFP and hemodynamic responses (CBV) was achieved by intravenously injecting a long-circulating red fluorescent dye, Rhodamine B. (**g-m**) Peri-stimulus heatmaps showing repeated trials and average response time-courses of the changes in measured rhoCBV, measured EYFP, derived HbO, derived HbR, corrected rhoCBV, corrected EYFP, and derived HbT, respectively. The gray-shaded segment indicates forepaw-stimulation period. (**n,o**) Correction of the contaminated EYFP and rhoCBV signals, respectively, across all subjects and all trials (n = 5, total trials = 30; $p < 0.001$, paired *t*-test). All color bars use the same unit as the time-course Y axis. Error bars represent standard deviation.

Impact of Hb-absorption on GCaMP signal measurement using fiber-photometry.

We virally expressed the GCaMP6f (hereafter as GCaMP), one of the most widely used genetically encoded calcium indicators, using AAV under the CaMKIIα promoter in S1FL. We also expressed tandem dimer tomato (tdTomato), a static red fluorescent protein, under the CAG promotor (**Fig. 2a, b**). Our rationale for choosing tdTomato was similar to that for EYFP in **Fig. 1**, as it does not encode activity changes and thus its photon counts can be used to derive ΔC_{HbO} and ΔC_{HbR} for GCaMP signal correction. Unlike in the experiment described in **Fig. 1**, Rhodamine B could no longer be used for CBV cross-validation because the red spectrum was occupied by tdTomato (**Fig. 2c**). Instead, we performed this GCaMP-tdTomato experiment inside a magnetic resonance imaging (MRI) scanner where CBV changes could be measured by intravenously administering an iron oxide contrast agent, Feraheme[23] (**Fig. 2d**). This allowed CBV to be validated using an established and completely independent modality. After a short, 1 s electrical stimulation of the contralateral forepaw (9 Hz, 3 mA, 0.5 ms pulse width), we observed a rapid increase in GCaMP signal followed by an undershoot (**Fig. 2e,q**). The tdTomato signal decreased significantly upon forepaw stimulation and showed a much longer delay in its kinetics (**Fig. 2f**). Using the methods identical to those for the experiment described in **Fig.1**, but with spectral photometry datapoints across 575-699 nm wavelengths over time, we derived $\Delta C_{HbO}(t)$ and $\Delta C_{HbR}(t)$ (**Fig. 2g, h**). Interestingly, the derived ΔC_{HbR} data exhibited a rapid initial increase (**Fig. 2h**) before a more prolonged reduction – a phenomenon well-documented in the optical literature[22] and termed "initial dip" in blood-oxygenation-level-dependent fMRI[23]. This initial increase in HbR was not detectable in the raw tdTomato data, indicating that our method is capable of deriving parameters with temporal kinetics distinct from the detected raw fluorescence activity. **Fig. 2j** shows the corrected GCaMP signals, where the after-stimulus undershoot no longer exists. Accordingly, **Fig. 2k** shows a flattened tdTomato trace following the correction. The derived $\Delta C_{HbT}(t)$ (**Fig. 2i**) highly resembled the CBV changes measured by fMRI (**Fig. 2l**) and these two time-courses correlated significantly (**Fig. 2m**). The derived ΔC_{HbT} showed higher sensitivity than MRI-CBV (**Fig. 2n**). We observed no significant time-lag between the ΔC_{HbT} and CBV-fMRI time-courses (**Fig. 2o, p**).

Fig. 2q and 2r demonstrate the corrections of pseudo-undershoot artifacts in GCaMP time-courses of short (1 s) and long (10 s) stimulations, respectively. These artifacts following short bursts of activation were also apparent when optogenetic stimulation was applied in the brain (**Extended Data Fig. 9**). In addition, we also observed a significant correction effect on GCaMP response amplitudes (**Extended Data Fig. 10**). Without proper correction of Hb-absorption artifacts, the accuracy of quantified fluorescence signals is compromised, leading to misinterpretation of fiber-photometry data. This problem could become exacerbated in the absence of time-locked stimulations, as the desired activity could be superimposed on physiological hemodynamic signal changes.

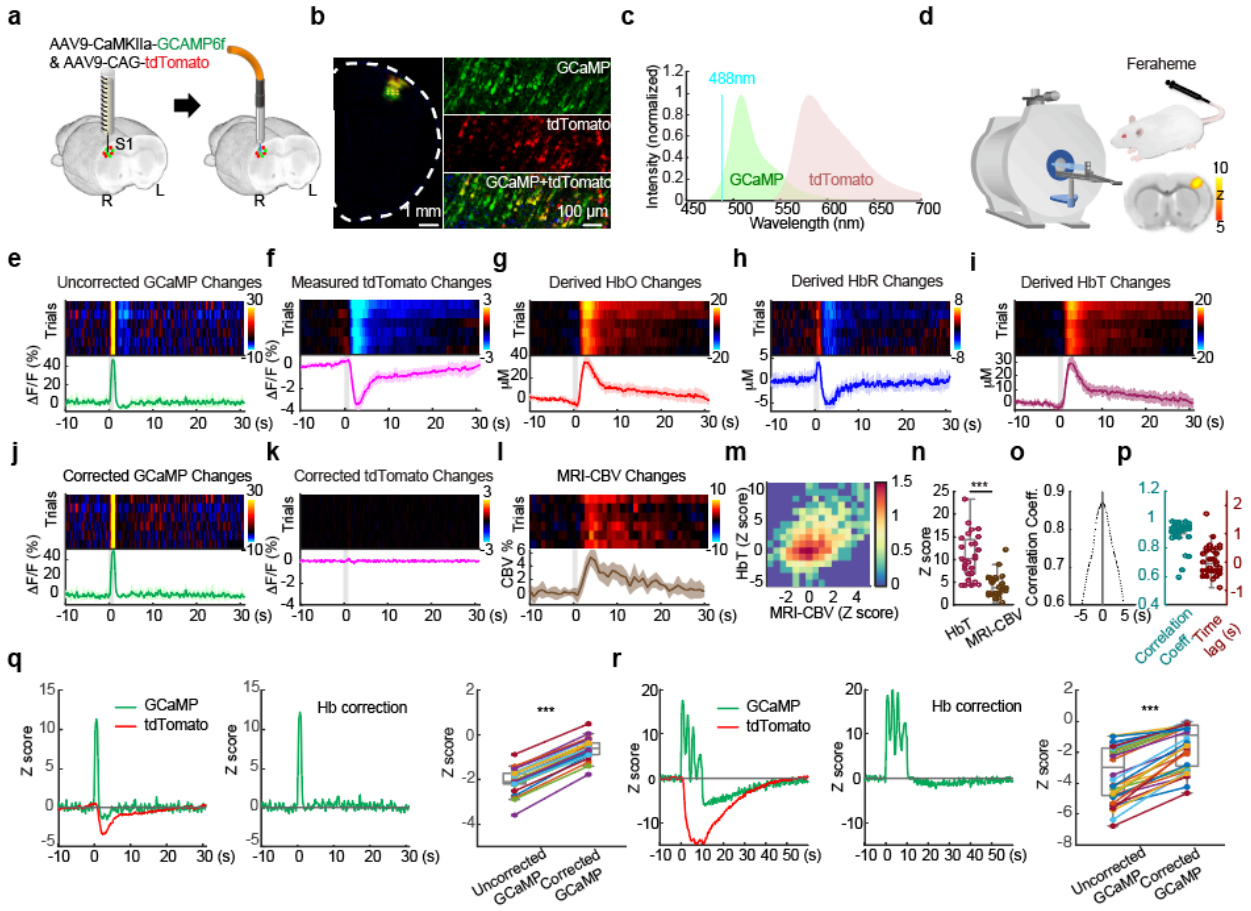

Fig. 2. Hb-absorption effects on GCaMP signal measurement using fiber-photometry (**a**) Fiber-photometry measurement of GCaMP and tdTomato signals in the S1 of the forelimb region. (**b**) Confocal images showing GCaMP and tdTomato expression. (**c**) GCaMP and tdTomato spectra. (**d**) CBV measurement was achieved by MRI and intravenous injection of the long-circulating iron oxide nanoparticle solution, Feraheme. Insert shows a forepaw-induced group-level fMRI activation map (n = 5). (**e-l**) Peri-stimulus heatmaps showing repeated trials and average response time-courses of the changes in measured GCaMP, measured tdTomato, derived HbO, derived HbR, derived

HbT, corrected GCaMP, corrected tdTomato, and measured MRI-CBV, respectively. The gray-shaded segment indicates the forepaw-stimulation period. (**m**) Two-dimensional histogram summarizing HbT and MRI-CBV changes across all subjects and all trials (n = 5, total trials = 27). Color bar indicates counts in log-scale. (**n**) Photometry derived HbT exhibited higher sensitivity than MRI-CBV. (**o**) Cross-correlation between the Z scores of the derived HbT and the Z scores of the MRI-CBV, with a representative cross-correlation coefficient plot over the peri-stimulus time period of 10 s, and (**p**) scatter plots of cross-correlation coefficients (left) and time lag (right) of all trials (n = 27). (**q,r**) Correction of pseudo-undershoot artifacts in GCaMP time-courses of **(q)** short (1 s), and **(r)** long (10 s) stimulations, respectively.

Brain regional differences in hemodynamic response function

Because our proposed technique allows simultaneous, Hb-artifact-free, accurate measurements of neuronal activity (e.g., GCaMP) and vascular responses (e.g., ΔC_{HbT}), it offers a significant added benefit towards studying the relationship between the two. This relationship, often termed the hemodynamic response function (HRF), governs the data interpretation of many noninvasive neuroimaging technologies such as fMRI, intrinsic optics, or functional ultrasound[24]. While the use of one canonical HRF to model activity throughout the brain remains the most common practice in the field, accumulating evidence shows that HRF is region-dependent[24,25] and that a thorough understanding of HRF affected by regional cell types, neurochemicals, and subject conditions is crucial to accurately interpret most neuroimaging data[26]. To demonstrate the utility of our proposed technique for computing region- and sensor-dependent HRFs, we first described the method to compute HRF (**Extended Data Fig. 11a**) and then validated the results on a dataset not used in HRF computation (**Extended Data Fig. 11b**). Next, we virally expressed GCaMP6f using AAV under the CaMKIIα promoter and tdTomato under the CAG promotor in the primary motor cortex (M1) of the left hemisphere and the caudate putamen (CPu, a.k.a. dorsal striatum) of the right hemisphere (**Fig. 3a, b**). We implanted a microelectrode into the M1 of the right hemisphere (**Fig. 3a**) such that transcallosal and corticostriatal stimulation could be achieved simultaneously. Upon electrical stimulation (60 Hz, 300 μA, 0.5 ms pulse width for 2 s), we observed robust GCaMP changes in the left M1 and right CPu (**Fig. 3c, d**), which are both monosynaptically connected to the stimulation target. Following the calculation of Hb concentration changes, Hb-absorption correction, and

computation of HRFs, we observed that M1 and CPu exhibited distinct HRF profiles (**Fig. 3c, d**). Interestingly, we also observed distinct HbR polarities between these two regions.

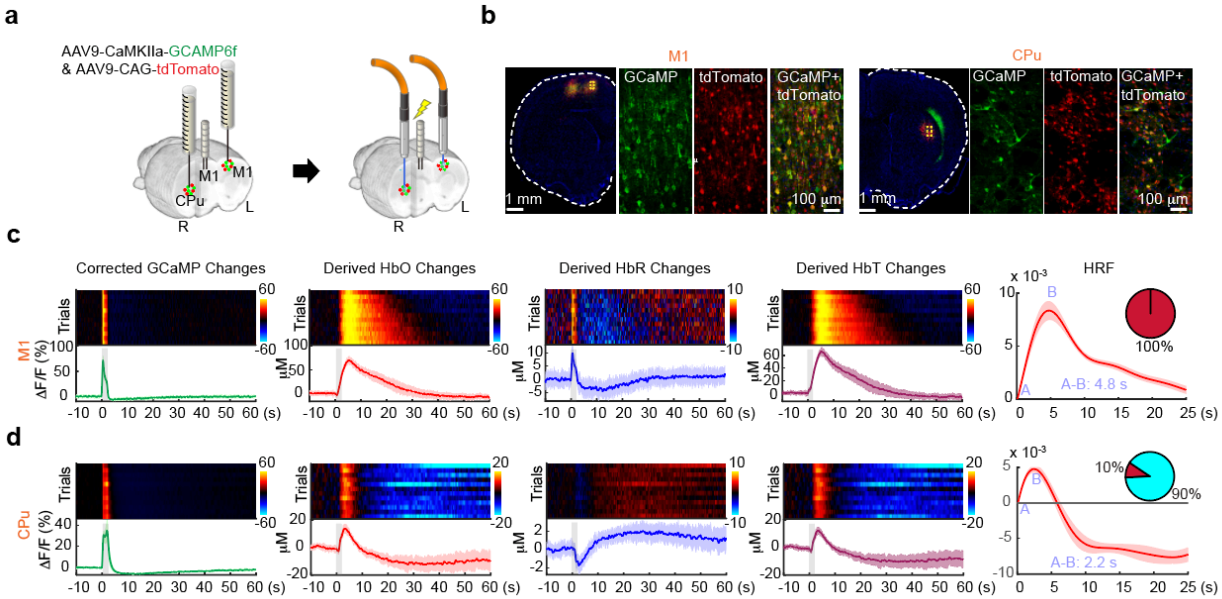

Fig. 3. Brain regional differences in hemodynamic response function (a) Fiber-photometry measurement of GCaMP and tdTomato signals in the left M1 and right CPu, both have direct anatomical connection with the right M1 receiving local microstimulation. (**b**) Confocal images showing GCaMP and tdTomato expression in M1 and CPu. (**c, d**) Peri-stimulus heatmaps and response time-courses of the changes in corrected GCaMP, derived HbO, derived HbR, and derived HbT, and the modeled HRFs in M1 and CPu, respectively. Inserted pie-charts indicate the ratio between positive (red) and negative (blue) HRF polarities. All per-stimulus heatmap color bars use the same unit as the time-course Y axis. Error bars represent standard deviation.

Discussion

Unlike many microscopy techniques that provide spatial information, fiber-photometry does not resolve fluorescence signals emitted from individual cells and its analysis cannot spatially circumvent around the blood vessels. Instead, fiber-photometry utilizes an optical fiber to collect all photons from the targeted volume (**Extended Data Fig. 4a-c**). With the conventional fiber-photometry setting, the targeted volume was reported to be $10^5 – 10^6$ µm^3 with a recording depth approximately at 200 µm from

the fiber tip [13]. Our simulated detection volume is well within this range (**Extended Data Fig. 12**). With the average blood volume fraction in the brain and Hb concentration documented in the literature[27], about 9860 μM Hb would appear within the photometry-detectable brain volume and affect the accuracy of fluorescent sensor measurement by absorbing both the excitation and emission photons. In a normal physiological condition, ΔC_{HbO} and ΔC_{HbT} could change for up to 40 μM[28] and CBV could change for up to ~20%[29] in response to neuronal activity, making such correction to be a time-dependent problem. Our derived changes in ΔC_{HbO} and ΔC_{HbT} (**Fig. 1i, m, Fig. 2g, i**), and measured rhoCBV (**Fig. 1k**), MRI-CBV (**Fig. 2l**) indeed support the amplitude of those changes are possible *in vivo*. Our data indicated that roughly 20% of CBV increase would contribute to 4.08% decrease of green fluorescent signal changes (**Extended Data Fig.13a,** 95% CI 1.33 - 6.83%), and 2.20% decrease of red fluorescent signal changes (**Extended Data Fig.13b,** 95% CI 0.57 - 3.84%). Such level of $\Delta F/F$ changes on both the green and red sensors are commonly reported in the photometry literature [30,31] and could be interpreted as the specific sensor activity changes when caution was not exercised. Conventionally, in the brain regions where CBV increases following local neuronal activation, a pseudo-negative fluorescent sensor activity would be expected. However, in cases where CBV decreases following neuronal activation, such as those reported in the CPu[32–34] or hippocampus[35], a pseudo-positive fluorescence signal would occur. Further, while several techniques are readily available to measure CBV [36–39] (**Fig. 1g,k, Fig. 2l**), the correction of Hb-absorption cannot be achieved by simply regressing the CBV signal measured concurrently (**Extended Data Fig. 14**). This is mainly because the absorption of HbO and HbR are wavelength dependent and their respective concentrations change over time [11,14] (**Extended Data Fig.1**). Our simulation suggested that the accuracy of fluorescent signal could be compromised even without a net CBV change (see **Extended Data Fig. 4d** for plots without shaded background). This makes it crucial to quantify both ΔC_{HbO} and ΔC_{HbR}, so that the true fluorescence signal changes can be restored.

Currently there are two major fluorescence-measurement-strategies in fiber-photometry. One is non-spectrally resolved using a narrow bandpass filter paired with a photodetector[2,40]. The other is

spectrally resolved using a photomultiplier tube array [6,41] or a spectrometer [1,31]. The non-spectrally resolved method has the advantage of collecting signals at higher frequency and can be used with modulated excitation lights and a lock-in amplifier[40]. In contrast, the spectrally resolved method provides wavelength-dependent information for the fluorescence where the detected photons can be matched with the specific spectral profile of the sensor to improve specificity, or perform spectral unmixing for multiplexing[1]. Our results support the use of spectrometer system for accurate measurement of fluorescence signals. However, if ΔC_{HbO} and ΔC_{HbR} cannot be obtained and a single non-spectral photodetector has to be used, our results indicated that far-red sensors are less prone to Hb absorption artifact (**Extended Data Fig 1 and 4d**). This highlights the importance to continually develop fluorescent sensors at the far-red range [42].

While our results unequivocally showed the necessity to correct for Hb-absorption artifacts, an ideal photometry recording platform should also be motion-artifact-free. Perhaps one strategy to achieve motion- and Hb-absorption-free recording of fluorescence signal is to express an activity-independent fluorescent protein in the far-red range so that motion-related artifacts can be regressed first, and Hb-absorption correction can follow to achieve a true fluorescence signal recording using fiber-photometry. This approach warrants further investigation and is therefore beyond the scope of the current study.

Meng et al. recently described the use of spectrally resolved fiber-photometry for simultaneous recording of calcium activities from direct and indirect medium spiny neurons in the CPu and found that both cell types coordinately control the dynamics of movement [1]. The opportunity to examine the interactions between cell types and/or neurotransmitters has become increasingly popular using fiber-photometry. If both the green and red spectrum are utilized to encode fluorescent sensor activities, it may be possible to use the spectral signals from the unmixing residuals (i.e., remaining autofluorescence) to achieve hemodynamic correction (**Extended Data Fig. 15**). Currently, this method suffers from signal-to-noise issues due to very low residual photon counts and is less appealing in our hands. However, this approach may demonstrate its utility with the advent of more sensitive spectrometer system or improved

unmixing algorithm. One additional approach that may be implemented to correct for Hb-absorption artifact is to utilize the GCaMP isosbestic point (400-410 nm), where excitation light delivered at this range would evoke GCaMP emission photons irrelevant to the changes of calcium concentration [43,44]. This correction method is built on the foundation that HbO and HbR both present significant absorption at the GCaMP isosbestic excitation wavelength as well as the corresponding emission wavelength. As a result, the fluorescent signal generated from GCaMP isosbestic excitation can be used as the static fluorescent reference signal in the analytical method proposed in this study and derive ΔC_{HbO} and ΔC_{HbR} to restore the functional GCaMP signals. The potential limitations with this approach are the trade-off in temporal resolution as interleaved excitation is required, a relatively low signal-to-noise (about one tenth of the emission signal as compared to that excited by the 488 nm excitation light), and the fact that this is a property unique to GCaMP but not all the other fluorescent sensors [45]. Our near-future work will focus on establishing an experimental pipeline to achieve motion and hemodynamic artifact-free measurement of a green and a red sensors (e.g., GCaMP and jRGECO) in freely-moving animals by incorporating a far-red static fluorescent sensor for motion correction followed by hemodynamic correction using data from isosbestic GCaMP excitation.

Given the irreplaceable roles of noninvasive hemodynamic-based neuroimaging techniques (such as fMRI, near-infrared, intrinsic optics, functional ultrasound, positron emission tomography, etc.) in studying brain function, identifying brain region-dependent HRF is crucial towards an accurate interpretation of hemodynamic-based neuroimaging data. Notably, the current standard fMRI analysis uses one HRF shape across the entire brain. Accumulating literature has pointed to the potential problems with this analysis pipeline because HRF is brain region dependent[25,46–48]. The current study and other pioneering studies[15,49–55] have together demonstrated that fiber-photometry could be seamlessly coupled with fMRI and provide ground-truth cellular activity to help unravel the relationship between neuronal and hemodynamic responses. These studies have bridged a crucial knowledge gap in interpreting fMRI data. The method proposed in this study further expands the scope of this research area, as it generates

hemodynamic signals "free-of-charge", with sensitivity better than fMRI (**Fig.2n**), and the results can be readily compared with the concurrently recorded fluorescent sensor activity. With the spectral photometry recording becoming increasingly popular, the proposed method opens up a unique opportunity to compute HRF in a cell-type dependent, stimulation-circuit dependent, neurotransmission-dependent, and behavior dependent manner. We expect that this information can be obtained by performing meta-analysis on spectral-photometry data shared through open-science platform and contribute significantly toward a more accurate interpretation of large-scale neuroimaging data.

In this study, we demonstrated that significant Hb-absorption artifacts in fiber-photometry data may cause inaccurate measurements and therefore erroneous interpretations. We proposed a method that addresses this issue by quantifying dynamic HbO and HbR absorption changes using activity-independent fluorescence spectra, and we demonstrated that these additional quantitative measurements were efficient in correcting the artifact and retrieve the desired, unperturbed fluorescence signals in fiber-photometry. This approach simultaneously measures HbO, HbR, and the activity of a selected fluorescent sensor, providing an additional experimental capability to investigate the influence of neuronal or neurochemical activity on cerebral hemodynamics. Through a proof-of-principle study, we provide direct evidence that HRF is brain-region dependent, suggesting that the analysis of hemodynamic-based neuroimaging data should not apply a single HRF across all brain regions.

Acknowledgements

We thank UNC CAMRI members and Dr. Elizabeth Hillman for their helpful discussions and critiques. We thank Drs. Lindsay Walton and Dom Cerri for editing the manuscript. This work is supported in part by NIH grants (RF1MH117053, R01MH111429, R01NS091236, P60AA011605, and U54HD079124 to Y.Y.I.S.), the Intramural Research Program of the NIH/NIEHS (1ZIAES103310 to G.C.), the Burroughs Wellcome Fund (CASI Award number 5113244 to N.C.P.), and the Arnold and Mabel Beckman Foundation (2021BYI to N.C.P.).

Author Contributions

W.-T.Z., T.-H.H.C., G.C., and Y.-Y.I.S. conceived the project and designed the experiments. W.-T.Z., T.-H.H.C., T.-W. W., E.A.O., J.Z., and R.N. implemented the methods. W.-T.Z., T.-H.H.C, Y.Y., S.-H.L., and N.C.P. analyzed data. W.-T.Z., T.-H.H.C, and Y.-Y.I.S. wrote the manuscript with input from all authors. H.Z., G.C, and Y-Y.I.S. supervised the study and provided funding support.

References

1. Meng, C. *et al.* Spectrally Resolved Fiber Photometry for Multi-component Analysis of Brain Circuits. *Neuron* **98**, 707-717 e4 (2018).
2. Kim, C. K. *et al.* Simultaneous fast measurement of circuit dynamics at multiple sites across the mammalian brain. *Nat. Methods* **13**, 325–328 (2016).
3. Chen, X. *et al.* Mapping optogenetically-driven single-vessel fMRI with concurrent neuronal calcium recordings in the rat hippocampus. *Nat. Commun.* **10**, 5239 (2019).
4. Pais-Roldán, P. *et al.* Indexing brain state-dependent pupil dynamics with simultaneous fMRI and optical fiber calcium recording. *Proc. Natl. Acad. Sci. U. S. A.* **117**, 6875–6882 (2020).
5. Wang, H., Jing, M. & Li, Y. Lighting up the brain: genetically encoded fluorescent sensors for imaging neurotransmitters and neuromodulators. *Curr. Opin. Neurobiol.* **50**, 171–178 (2018).
6. Cui, G. *et al.* Concurrent Activation of Striatal Direct and Indirect Pathways During Action Initiation. *Nature* **494**, 238–242 (2013).
7. Sych, Y., Chernysheva, M., Sumanovski, L. T. & Helmchen, F. High-density multi-fiber photometry for studying large-scale brain circuit dynamics. *Nat. Methods* **16**, 553–560 (2019).
8. Pisano, F. *et al.* Depth-resolved fiber photometry with a single tapered optical fiber implant. *Nat. Methods* **16**, 1185–1192 (2019).
9. Luchsinger, J. R. *et al.* Delineation of an insula-BNST circuit engaged by struggling behavior that regulates avoidance in mice. *Nat. Commun.* **12**, 3561 (2021).
10. Ma, Y. *et al.* Wide-field optical mapping of neural activity and brain haemodynamics: considerations and novel approaches. *Philos. Trans. R. Soc. Lond. B. Biol. Sci.* **371**, (2016).

11. Prahl, S. Optical Absorption of Hemoglobin. http://omlc.org/spectra/hemoglobin.

12. Smith, A. F. *et al.* Brain Capillary Networks Across Species: A few Simple Organizational Requirements Are Sufficient to Reproduce Both Structure and Function. *Front. Physiol.* **10**, 233 (2019).

13. Pisanello, M. *et al.* The Three-Dimensional Signal Collection Field for Fiber Photometry in Brain Tissue. *Front. Neurosci.* **13**, 82 (2019).

14. Meng, F. & Alayash, A. I. Determination of extinction coefficients of human hemoglobin in various redox states. *Anal. Biochem.* **521**, 11–19 (2017).

15. Schulz, K. *et al.* Simultaneous BOLD fMRI and fiber-optic calcium recording in rat neocortex. *Nat Methods* **9**, 597–602 (2012).

16. Hillman, E. M. C. Optical brain imaging in vivo: techniques and applications from animal to man. *J. Biomed. Opt.* **12**, 051402–051402 (2007).

17. Rungta, R. L., Osmanski, B.-F., Boido, D., Tanter, M. & Charpak, S. Light controls cerebral blood flow in naive animals. *Nat. Commun.* **8**, 14191 (2017).

18. Hansen, L. P. Large Sample Properties of Generalized Method of Moments Estimators. *Econometrica* **50**, 1029–1054 (1982).

19. Unekawa, M. *et al.* Hyperperfusion counteracted by transient rapid vasoconstriction followed by long-lasting oligemia induced by cortical spreading depression in anesthetized mice. *J. Cereb. Blood Flow Metab. Off. J. Int. Soc. Cereb. Blood Flow Metab.* **35**, 689–698 (2015).

20. Vasanawala, S. S. *et al.* Safety and technique of ferumoxytol administration for MRI. *Magn. Reson. Med.* **75**, 2107–2111 (2016).

21. Wei, H. *et al.* Exceedingly small iron oxide nanoparticles as positive MRI contrast agents. *Proc. Natl. Acad. Sci. U. S. A.* **114**, 2325–2330 (2017).

22. Devor, A. *et al.* Coupling of total hemoglobin concentration, oxygenation, and neural activity in rat somatosensory cortex. *Neuron* **39**, 353–359 (2003).

23. Hu, X. & Yacoub, E. The story of the initial dip in fMRI. *NeuroImage* **62**, 1103–1108 (2012).

24. Taylor, A. J., Kim, J. H. & Ress, D. Characterization of the hemodynamic response function across the majority of human cerebral cortex. *NeuroImage* **173**, 322–331 (2018).

25. Devonshire, I. M. *et al.* Neurovascular coupling is brain region-dependent. *Neuroimage* **59**, 1997–2006 (2012).

26. Lecrux, C. & Hamel, E. Neuronal networks and mediators of cortical neurovascular coupling responses in normal and altered brain states. *Philos Trans R Soc Lond B Biol Sci* **371**, (2016).

27. van Zijl, P. C. *et al.* Quantitative assessment of blood flow, blood volume and blood oxygenation effects in functional magnetic resonance imaging. *Nat. Med.* **4**, 159–167 (1998).

28. Hillman, E. M. Coupling mechanism and significance of the BOLD signal: a status report. *Annu Rev Neurosci* **37**, 161–81 (2014).

29. Uludağ, K. & Blinder, P. Linking brain vascular physiology to hemodynamic response in ultra-high field MRI. *NeuroImage* **168**, 279–295 (2018).

30. Chen, T. W. *et al.* Ultrasensitive fluorescent proteins for imaging neuronal activity. *Nature* **499**, 295–300 (2013).

31. Sun, F. *et al.* A Genetically Encoded Fluorescent Sensor Enables Rapid and Specific Detection of Dopamine in Flies, Fish, and Mice. *Cell* **174**, 481-496.e19 (2018).

32. Shih, Y. Y. *et al.* A new scenario for negative functional magnetic resonance imaging signals: endogenous neurotransmission. *J Neurosci* **29**, 3036–44 (2009).

33. Shih, Y.-Y. I., Wey, H.-Y., De La Garza, B. H. & Duong, T. Q. Striatal and cortical BOLD, blood flow, blood volume, oxygen consumption, and glucose consumption changes in noxious forepaw electrical stimulation. *J. Cereb. Blood Flow Metab. Off. J. Int. Soc. Cereb. Blood Flow Metab.* **31**, 832–841 (2011).

34. Shih, Y.-Y. I. *et al.* Imaging neurovascular function and functional recovery after stroke in the rat striatum using forepaw stimulation. *J. Cereb. Blood Flow Metab. Off. J. Int. Soc. Cereb. Blood Flow Metab.* **34**, 1483–1492 (2014).

35. Schridde, U. *et al.* Negative BOLD with large increases in neuronal activity. *Cereb. Cortex N. Y. N 1991* **18**, 1814–1827 (2008).

36. Kwong, K. K. *et al.* Dynamic magnetic resonance imaging of human brain activity during primary sensory stimulation. *Proc Natl Acad Sci U A* **89**, 5675–9 (1992).

37. Sakai, F. *et al.* Regional cerebral blood volume and hematocrit measured in normal human volunteers by single-photon emission computed tomography. *J. Cereb. Blood Flow Metab. Off. J. Int. Soc. Cereb. Blood Flow Metab.* **5**, 207–213 (1985).

38. Mintun, M. A., Raichle, M. E., Martin, W. R. & Herscovitch, P. Brain oxygen utilization measured with O-15 radiotracers and positron emission tomography. *J. Nucl. Med. Off. Publ. Soc. Nucl. Med.* **25**, 177–187 (1984).

39. Siegel, A. M., Culver, J. P., Mandeville, J. B. & Boas, D. A. Temporal comparison of functional brain imaging with diffuse optical tomography and fMRI during rat forepaw stimulation. *Phys. Med. Biol.* **48**, 1391–1403 (2003).

40. Gunaydin, L. A. *et al.* Natural neural projection dynamics underlying social behavior. *Cell* **157**, 1535–1551 (2014).

41. Cui, G. *et al.* Deep brain optical measurements of cell type-specific neural activity in behaving mice. *Nat Protoc* **9**, 1213–28 (2014).

42. Patriarchi, T. *et al.* An expanded palette of dopamine sensors for multiplex imaging in vivo. *Nat. Methods* **17**, 1147–1155 (2020).

43. Lerner, T. N. *et al.* Intact-Brain Analyses Reveal Distinct Information Carried by SNc Dopamine Subcircuits. *Cell* **162**, 635–647 (2015).

44. Allen, W. E. *et al.* Global Representations of Goal-Directed Behavior in Distinct Cell Types of Mouse Neocortex. *Neuron* **94**, 891-907.e6 (2017).

45. Sun, F. *et al.* Next-generation GRAB sensors for monitoring dopaminergic activity in vivo. *Nat. Methods* **17**, 1156–1166 (2020).

46. Sloan, H. L. *et al.* Regional differences in neurovascular coupling in rat brain as determined by fMRI and electrophysiology. *NeuroImage* **53**, 399–411 (2010).

47. Jin, M. *et al.* Disturbed neurovascular coupling in hemodialysis patients. *PeerJ* **8**, e8989 (2020).

48. Ekstrom, A. D. Regional variation in neurovascular coupling and why we still lack a Rosetta Stone. *Philos. Trans. R. Soc. Lond. B. Biol. Sci.* **376**, 20190634 (2021).

49. Schmid, F. *et al.* Assessing sensory versus optogenetic network activation by combining (o)fMRI with optical Ca2+ recordings. *J Cereb Blood Flow Metab* **36**, 1885–1900 (2016).

50. Schwalm, M. *et al.* Cortex-wide BOLD fMRI activity reflects locally-recorded slow oscillation-associated calcium waves. *Elife* **6**, (2017).

51. Liang, Z., Ma, Y., Watson, G. D. R. & Zhang, N. Simultaneous GCaMP6-based fiber photometry and fMRI in rats. *J Neurosci Methods* **289**, 31–38 (2017).

52. Albers, F., Wachsmuth, L., van Alst, T. M. & Faber, C. Multimodal Functional Neuroimaging by Simultaneous BOLD fMRI and Fiber-Optic Calcium Recordings and Optogenetic Control. *Mol. Imaging Biol.* (2017) doi:10.1007/s11307-017-1130-6.

53. Schlegel, F. *et al.* Fiber-optic implant for simultaneous fluorescence-based calcium recordings and BOLD fMRI in mice. *Nat Protoc* **13**, 840–855 (2018).

54. He, Y. *et al.* Ultra-Slow Single-Vessel BOLD and CBV-Based fMRI Spatiotemporal Dynamics and Their Correlation with Neuronal Intracellular Calcium Signals. *Neuron* **97**, 925-939.e5 (2018).

55. Wang, M., He, Y., Sejnowski, T. J. & Yu, X. Brain-state dependent astrocytic Ca(2+) signals are coupled to both positive and negative BOLD-fMRI signals. *Proc. Natl. Acad. Sci. U. S. A.* **115**, E1647–E1656 (2018).

56. Henyey, L. G. & Greenstein, J. L. Diffuse radiation in the galaxy. *Astrophys J* **93**, 70–83 (1941).

57. Zhao, Y., Qiu, L., Sun, Y., Huang, C. & Li, T. Optimal hemoglobin extinction coefficient data set for near-infrared spectroscopy. *Biomed. Opt. Express* **8**, 5151–5159 (2017).

58. Shih, Y. Y. *et al.* Pharmacological MRI of the choroid and retina: blood flow and BOLD responses during nitroprusside infusion. *Magn Reson Med* **68**, 1273–8 (2012).

59. Shih, Y.-Y. I. *et al.* Quantitative retinal and choroidal blood flow during light, dark adaptation and flicker light stimulation in rats using fluorescent microspheres. *Curr. Eye Res.* **38**, 292–298 (2013).

60. Cox, R. W. AFNI: software for analysis and visualization of functional magnetic resonance neuroimages. *Comput. Biomed. Res. Int. J.* **29**, 162–173 (1996).

61. Worsley, K. J. & Friston, K. J. Analysis of fMRI time-series revisited--again. *NeuroImage* **2**, 173–181 (1995).

62. Valdés-Hernández, P. A. *et al.* An in vivo MRI Template Set for Morphometry, Tissue Segmentation, and fMRI Localization in Rats. *Front. Neuroinformatics* **5**, 26 (2011).

63. Decot, H. K. *et al.* Coordination of Brain-Wide Activity Dynamics by Dopaminergic Neurons. *Neuropsychopharmacol. Off. Publ. Am. Coll. Neuropsychopharmacol.* **42**, 615–627 (2017).

Methods

KEY RESOURCES TABLE

REAGENT OR RESOURCE	SOURCE	IDENTIFIER
Recombinant DNA		
AAV5-CaMKIIα-EYFP	UNC Vector Core	N/A
AAV9-CaMKIIα-GCaMP6f-WPRE-SV40	U.Penn Vector Core	AV-9-PV3435
AAV9-CAG-tdTomato	UNC Vector Core	N/A
AAV9-CaMKIIα-ChR2-EYFP	UNC Vector Core	N/A
Software and Algorithms		
Matlab	Mathworks	R2019b
RStudio	RStudio Inc.	Version 1.0.136
Other		
488 nm laser and remote	Coherent	OBIS 488 LS (60 mW)
561 nm laser and remote	Coherent	OBIS 561 LS (50 mW)
Spectrometer	Ocean Optics	QE-pro
Optic patch cable	Thorlabs	FT200EMT (200 mm, 0.39 NA)
Uncleaved fiber optic cannula	Thorlabs	CFMC12U-20 (200 mm, 0.39 NA)
Bipolar Tungsten electrode	P1 Technologies	MS303T/2C-B/SP ELEC .008/.2MM TW TUNGSTEN (MRI)

Monte Carlo simulation for photon transport in fiber-photometry recording

The Monte Carlo simulation of photon transport during fiber-photometry recording was achieved in two steps: 1) excitation light path simulation and 2) emission light path simulation. The goal was to first build a database composed of a large number of possible excitation light paths. After which, an emission starting point can be randomly selected from the excitation light path database for emission light path simulation.

For the excitation light path simulation, we built the database by repeatedly launching excitation photon packets that started with a unity weight = 1. The photon packets deposited weight due to absorption at each step of traveling through the simulated brain, and the photon packet's current locations and remaining weights were logged along the way. Each excitation photon packet repeatedly underwent the following steps (**Extended Data Fig.2**, left panel), until it was either terminated or transmitted out of the brain.

Step 1: Launching a photon packet (**Extended Data Fig.2**, left panel a and b):

In our model, we launched our photon packets from an optic fiber tip with a diameter of 200 µm; the range of possible launch directions, or so-called acceptance angles, would be limited by the fiber numerical aperture (NA) according to Snell's law. For applications, the NA is most commonly expressed as:

$$NA_{fiber} = n_i \sin \theta_a \tag{2}$$

where θ_a is the maximum 1/2 acceptance angle of the fiber, and n_i is the index of refraction of the material outside of the fiber. With this in mind, we simply set the initial launch position randomly within the surface of fiber tip, along with a random initial launch direction that was within the range of acceptance angles. This can be easily done by using three Cartesian coordinates (x, y, z) and three direction cosines (v_x, v_y, v_z) to determine the initial position and direction, respectively.

For initial position:

$$x = r_{fiber}\sqrt{\xi_1}\cos(2\pi\xi_2)$$

$$y = r_{fiber}\sqrt{\xi_1}\sin(2\pi\xi_2)$$

$$z = 0 \tag{3}$$

For initial direction:

$$v_x = \sin(\theta_a\xi_3)\cos(2\pi\xi_4)$$

$$v_y = \sin(\theta_a\xi_3)\sin(2\pi\xi_4)$$

$$v_z = \cos(\theta_a\xi_3) \tag{4}$$

where r_{fiber} is the radius of the optic fiber, and ξ_{1-4} are the independent random numbers between 0 and 1.

Step 2: Step size selection and photon packet movement (**Extended Data Fig. 2**, left panel 1-2 and right panel 5-6):

The step size s is the distance that the photon packet travels between interaction sites. In our study, we selected a step size using the following function derived from the inverse distribution method and the Beer–Lambert law:

$$s = -\frac{\ln\xi}{\mu_t} \tag{5}$$

where ξ is a random number between 0 and 1, and μ_t is the total interaction coefficient (the sum of the absorption coefficient (μ_a) and scattering coefficient (μ_s) of brain tissue). The μ_a and μ_s for distinct wavelengths of a traveling photon were derived from the optical absorption and scattering properties

provided by an online database from Oregon Medical Laser Center, Oregon Health & Science University (https://omlc.org/software/mc/mcxyz/index.html). We assumed 3% blood with 75% average oxygen saturation in our simulated brain.

Once the step size was selected, the photon packet traveled for distance s in the direction defined by direction cosines, and the coordinates were updated as follows:

$$x \leftarrow x + v_x s$$

$$y \leftarrow y + v_y s$$

$$z \leftarrow z + v_z s \tag{6}$$

Step 3: Absorption and scattering (**Extended Data Fig. 2**, left panel 3-4 and right panel 7-8):

At each interaction site, photon weight was partially absorbed by brain tissue, and the decreased fraction of the weight Δw can be defined as:

$$\Delta w = w(1 - e^{-\mu_a s}) \tag{7}$$

The weight of the photon packet was then updated as follows:

$$w \leftarrow w - \Delta w \tag{8}$$

Following absorption, the photon packet was scattered. The scattering direction was defined by both scattering angle θ and polar angle φ. The scattering angle was determined using the Henyey-Greenstein phase function[56]:

$$\cos\theta = \begin{cases} \frac{1}{2g}\left[1 + g^2 - \left(\frac{1 - g^2}{1 - g + 2g\xi}\right)^2\right] & if\ g \neq 0 \\ 1 - 2\xi & if\ g = 0 \end{cases} \tag{9}$$

where g refers to scattering anisotropy, which has a value between −1 and 1. When g is 0, it generally indicates that the scattering is isotropic. As g approaches 1 or -1, the scattering is confined to forwards and backwards, respectively.

The polar angle was assumed to be uniformly distributed between 0 and 2π, as below:

$$\varphi = 2\pi\xi \tag{10}$$

With these angles and the original direction cosines, we were able to calculate the new set of propagation direction cosines, which can be represented in the global coordinate system as follows:

$$v'_x = \begin{cases} \dfrac{\sin\theta\left(v_x v_z \cos\varphi - v_y \sin\varphi\right)}{\sqrt{1-v_z^2}} + \mu_x \cos\theta & if\ v_z \neq 1 \cap \mu_z \neq -1 \\ \sin\theta\cos\varphi & if\ v_z = 1 \cup \mu_z = -1 \end{cases}$$

$$v'_y = \begin{cases} \dfrac{\sin\theta\left(v_y v_z \cos\varphi - v_x \sin\varphi\right)}{\sqrt{1-v_z^2}} + \mu_y \cos\theta & if\ v_z \neq 1 \cap \mu_z \neq -1 \\ \sin\theta\sin\varphi & if\ v_z = 1 \\ -\sin\theta\sin\varphi & if\ v_z = -1 \end{cases}$$

$$v'_z = \begin{cases} -\sqrt{1-v_z^2}\sin\theta\cos\varphi + v_z\cos\theta & if\ v_z \neq 1 \cap \mu_z \neq -1 \\ \cos\theta & if\ v_z = 1 \\ -\cos\theta & if\ v_z = -1 \end{cases} \tag{11}$$

Step 4: Photon termination

Steps 2 and 3 were repeated until the weight of the photon packet reached 10^{-4} or less, then the simulation for this particular photon packet was terminated. The excitation light path and weight of each step were saved to the database, after which a new photon packet simulation was started from step 1.

The emission light path simulation was similar to the excitation light path simulation. Specifically, we need to first determine the initial position, the initial direction, and the initial weight before launching an emission photon packet (**Extended Data Fig. 2**, right panel c-d). The initial coordinates of each emission

photon packet were randomly selected from the excitation light path database. All coordinates in the database had an equal probability to be selected regardless of excitation light path. If the selected coordinates were within an area containing fluorophore, its initial coordinates were determined first, and then the corresponding excitation light path history (from the start to the point where the emission occurred) was recorded. In this study, we assumed the fluorophore existed equally within a 1 mm diameter sphere of viral expression area centered 0.3 mm below the fiber tip.

The initial direction of an emission photon was assumed to have isotropic probability in all directions; therefore, the direction cosines can be derived using the following:

$$v_x = \sin(\pi\xi_1)\cos(2\pi\xi_2)$$

$$v_y = \sin(\pi\xi_1)\sin(2\pi\xi_2)$$

$$v_z = \cos(\pi\xi_1) \tag{12}$$

Lastly, the initial weights were inherited from the remaining weights of the excitation photon packet at the initial coordinates.

Steps 2 and 3 were repeated until the weight of the photon packet reached 10^{-4} or less, and then the simulation of this photon packet was terminated (step 4). In emission step 4, only when the photon packet reached the fiber tip at smaller than 1/2 acceptance angle and a weight beyond 10^{-4}, the paired excitation/emission light path and the weight of each step were saved to the database. In order to improve signal-to-noise ratio, we collected 2-2.5 $\times$ 10^4 pairs of excitation and emission light paths.

The final weight (W_{final}) when the emission photon reaching the optical fiber tip represents the survival rate of the current combined excitation/emission light path. Therefore, the total average pathlength of excitation and emission lights are then calculated by summing each survived photon's W_{final} multiplied by its paired excitation and emission pathlength respectively:

$$\bar{X}_{ex}(\lambda_{em}) = \sum_{n=1}^{N} X_{ex}(n) \cdot e^{-\mu_a(\lambda_{ex})\cdot X_{ex}(n)} \cdot e^{-\mu_a(\lambda_{em})\cdot X_{em}(n)} = \sum_{n=1}^{N} X_{ex}(n) \cdot W_{final}$$

$$\bar{X}_{em}(\lambda_{em}) = \sum_{n=1}^{N} X_{em}(n) \cdot e^{-\mu_a(\lambda_{ex})\cdot X_{ex}(n)} \cdot e^{-\mu_a(\lambda_{em})\cdot X_{em}(n)} = \sum_{n=1}^{N} X_{em}(n) \cdot W_{final} \qquad (13)$$

Since the W_{final} is affected during both excitation and emission phase, the emission measured at different wavelengths have not only distinct average emission pathlength ($\bar{X}_{em}(\lambda_{em})$), but also distinct average excitation pathlength ($\bar{X}_{ex}(\lambda_{em})$) even when these emission wavelengths are excited by the same excitation wavelength. In this study, only the 488 nm excitation wavelength was used and simulated.

To plot the 488 nm excitation light illuminating distribution (Extended Data Fig. 3a), all excitation light paths' coordinates generated from the excitation light path simulation, regardless to the emission light detection, were first compressed into 2D coordinates, and then used for the 2D histogram. To plot the 515 or 580 nm emission light receptive probability map (Extended Data Fig. 3b-c), the initial emission 3D coordinate of each successfully detected 515 or 580 emission photons were compressed into 2D coordinates and shown in a 2D histogram.

Correction of Hb-absorption

Given the different absorption of HbO and HbR (**Extended Data Fig. 1a**), their dynamic concentration changes must be quantified in order to properly correct fluorescent sensor signals. To address this, we proposed the following methods to derive HbO and HbR concentration (ΔC_{HbO} and ΔC_{HbR}) time-courses using spectral datapoints.

In a simple, non-absorbing and non-scattering medium, the measured fluorescence signal *F* at any time *t* is linearly related to the fluorescent protein concentration $C(t)$:

$$\frac{F(t)}{F(t_0)} = \frac{C(t)}{C(t_0)} \qquad (14)$$

where $F(t_0)$ and $C(t_0)$ represent the fluorescence signal and the fluorescent protein concentration at the reference time point *0*, respectively. When the absorption of the medium is considered, and *F* is measured at multiple wavelengths λ_{Em}, equation (13) can be further modified according to an established model[10]:

$$\frac{F(t,\lambda_{Em})}{F(t_0,\lambda_{Em})} = e^{-[\Delta\mu_a(t,\lambda_{Ex})X(\lambda_{Ex})+\Delta\mu_a(t,\lambda_{Em})X(\lambda_{Em})]} \cdot \frac{C(t)}{C(t_0)} \tag{15}$$

where $\Delta\mu_a(t,\lambda_{Ex})$ represents the change of the absorption coefficient μ_a at excitation wavelength λ_{Ex} at the time point *t* compared to the time point *0*; $\Delta\mu_a(t,\lambda_{Em})$ represents the change of the absorption coefficient μ_a at emission wavelength λ_{Em} at the time point *t* compared to the time point *0*; $X(\lambda_{Ex})$ and $X(\lambda_{Em})$ represent the photon traveling pathlengths at the given wavelength, respectively. Next, HbO and HbR concentration changes (ΔC_{HbO} and ΔC_{HbR}) as a function of time need to be incorporated. When using 488 nm excitation, the absorption term in equation (14) that contains $\Delta\mu_a$ could be expressed as:

$$\begin{aligned}
&\Delta\mu_\alpha(t,\lambda_{\mathrm{Ex}})X(\lambda_{\mathrm{Ex}}) + \Delta\mu_\alpha(t,\lambda_{\mathrm{Em}})X(\lambda_{\mathrm{Em}}) \\
&\qquad = \Delta\mu_\alpha(t,488\,nm)X(488\,nm) + \Delta\mu_\alpha(t,\lambda_{\mathrm{Em}})X(\lambda_{\mathrm{Em}}) \\
&\approx [\xi_{HbO}(488\,nm)\,\Delta\,C_{HbO}(t) + \xi_{HbR}(488\,nm)\,\Delta\,C_{HbR}(t)]X(488\,nm) \\
&\qquad + [\xi_{HbO}(\lambda_{Em})\,\Delta\,C_{HbO}(t) + \xi_{HbR}(\lambda_{Em})\,\Delta\,C_{HbR}(t)]X(\lambda_{Em}) \\
&= \Delta\,C_{HbO}(t)[\xi_{HbO}(488\,nm)X(488\,nm) + \xi_{HbO}(\lambda_{Em})X(\lambda_{Em})] + \\
&\qquad \Delta\,C_{HbR}(t)[\xi_{HbR}(488\,nm)X(488\,nm) + \xi_{HbR}(\lambda_{Em})X(\lambda_{Em})]
\end{aligned} \tag{16}$$

where ξ_{HbO} and ξ_{HbR} are well-established molar extinction coefficients at different wavelengths of HbO and HbR, respectively[11].

At the time point *t*, the measured fluorescence ratio after natural logarithmic transformation, ranged from λ_{Em_1} to λ_{Em_n} could be put together in a vector form $M(t)$:

$$\mathrm{M}(t) = \begin{bmatrix} ln\left(\frac{F(t,\lambda_{Em_1})}{F(0,\lambda_{Em_1})}\right) \\ \vdots \\ \vdots \\ ln\left(\frac{F(t,\lambda_{Em_n})}{F(0,\lambda_{Em_n})}\right) \end{bmatrix} \tag{17}$$

Additionally, two vectors A and B could be used to represent the following:

$$A = \xi_{HbO}(488nm) \cdot X(488nm) + \begin{bmatrix} \xi_{HbO}(\lambda_{Em_1}) \cdot X(\lambda_{Em_1}) \\ \vdots \\ \vdots \\ \xi_{HbO}(\lambda_{Em_n}) \cdot X(\lambda_{Em_n}) \end{bmatrix} \tag{18}$$

$$B = \xi_{HbR}(488nm) \cdot X(488nm) + \begin{bmatrix} \xi_{HbR}(\lambda_{Em_1}) \cdot X(\lambda_{Em_1}) \\ \vdots \\ \vdots \\ \xi_{HbR}(\lambda_{Em_n}) \cdot X(\lambda_{Em_n}) \end{bmatrix} \tag{19}$$

With any activity-independent static fluorescence signals, the last component $\ln\frac{C(t)}{C(t_0)}$ should be 0. Practically, we designate an error value σ. Taken together, equation (14) could then be simplified and reorganized as equation (19). To solve $\Delta C_{HbO}(t)$ and $\Delta C_{HbR}(t)$ at any time point *t*, we used generalized method of moment (GMM)[18] to minimize L in equation (20). By performing the GMM computation for each time point, we can obtain a time series of $\Delta C_{HbO}(t)$, $\Delta C_{HbR}(t)$ and σ.

$$M(t) + \Delta C_{HbO}(t) \cdot A + \Delta C_{HbR}(t) \cdot B - \sigma = 0 \tag{20}$$

$$\mathrm{L} = \sum_{i=1}^{n} (M(t)_i + \Delta C_{HbO}(t) \cdot A_i + \Delta C_{HbR}(t) \cdot B_i - \sigma)^2 \tag{21}$$

In this case, we have numerous spectral datapoints that can be used to resolve two unknowns that are of interest (**Extended Data Fig. 5**) – $\Delta C_{HbO}(t)$ and $\Delta C_{HbR}(t)$. After which, $\Delta\mu_\alpha(t,\lambda_{\mathrm{Ex}})$ and

$\Delta\mu_\alpha(t, \lambda_{\mathrm{Em}})$ can be calculated using equation (15) and $F(t, \lambda_{Em})$ can be subsequently calculated using equation (14) to correct for HbO and HbR absorptions.

Subject

This study employed a total of 14 male Sprague Dawley (SD) rats weighing between 300-600g. All procedures were performed in accordance with the National Institutes of Health Guidelines for Animal Research (Guide for the Care and Use of Laboratory Animals) and approved by the University of North Carolina (UNC) Institutional Animal Care and Use Committee. These rats were separated into four cohorts. In the first cohort (n=3), EYFP was expressed in the bilateral S1FL using AAV5-CaMKIIα-EYFP (titer 4.2×10^{12} molecules/mL, UNC Vector Core) to demonstrate the impact of Hb concentration changes on static fluorescence signals and evaluate the proposed correction method. In the second cohort (n=4), GCaMP and tdTomato were co-expressed in the bilateral S1FL using a mixture of AAV9-CaMKIIα-GCaMP6f-WPRE-SV40 (titer $\geq 1 \times 10^{13}$ vg/mL, Penn Vector Core) and AAV9-CAG-tdTomato (titer 3.8×10^{12} molecules/mL, UNC Vector Core) at 5:1 ratio to demonstrate the impact of Hb concentration changes on a commonly used fluorescent sensor and evaluate the proposed correction method. The third cohort (n=4) received a twisted tungsten electrode implanted into the M1, and GCaMP and tdTomato were co-expressed in the contralateral M1 and ipsilateral striatum using a viral mixture identical to the second cohort. The fourth cohort (n=3) was used in a supplementary study, and had channelrhodopsin2 (ChR2) expressed in the ventroposterior thalamus (VP) using AAV9-CaMKIIα-ChR2-EYFP (titer 3.6×10^{12} molecules/mL, UNC Vector Core) and GCaMP expressed in the ipsilateral S1 using AAV9-CaMKII-GCaMP6f-WPRE-SV40 (titer $\geq 1 \times 10^{13}$ vg/mL, Penn Vector Core). All rats in this study were housed under environmentally-controlled conditions (12 h normal light/dark cycles, lights on at 7am; 20–23 °C and 40–60% relative humidity), with ad libitum access to food and water.

Stereotactic surgery

For all surgical procedures, rats were anesthetized initially by 5% isoflurane, and maintained by a constant flow of 2-3% isoflurane mixed with medical air. Rectal temperature was continuously monitored and maintained within 37 ± 0.5 °C using a feedback-controlled heating pad (Harvard Apparatus, Model 557020, Holliston, MA). Rats were head-fixed to a stereotactic frame (Kopf Instruments, Model 962, Tujunga, CA). The skin was opened to expose the skull surface, and burr holes were prepared according to experimental coordinates. All coordinates used for microinjection are listed as follows. S1: AP = +0.5 mm and ML = +3.7 mm, DV = 1.3 mm, M1: AP = +1.8 mm and ML = -2.5 mm, DV = 2.0 mm, Striatum: AP = 0.5 mm and ML = 4.0 mm, DV = 5.2 mm, VP: AP = -2.8 mm and ML = +2.5 mm, DV = 6.5 mm. Microinjections were performed at a flow rate of 0.1 μL/min for 1 μL, and an additional 10 min was given for virus diffusion prior to slow retraction of the microsyringe needle. The burr holes were then sealed with bone wax (Fisher Scientific, Pittsburgh, PA), and the wound was sutured. A month after the virus microinjection, the skin was reopened to expose the skull, then the bone wax was removed and optical fibers (200 μm in diameter; NA: 0.39) were chronically implanted to coordinates 0.2-0.5 mm above the virus injection sites. Four MR-compatible miniature brass screws (Item #94070A031, McMaster Carr, Atlanta, GA) were anchored to the skull, then the surface of the skull was covered with dental cement to seal implanted components and the wound was sutured to further protect the surgical site.

At the end of every surgical procedure, lidocaine jelly (#866096, Henry Schein Inc., Melville, NY) was applied around the surgical wound for pain relief, and to prevent the rat scratching the wound. Meloxicam (#6451720670, Henry Schein Inc., Melville, NY) was also given by oral administration for further pain relief. Rats were allowed at least 1 week for recovery from surgical procedures before any further experiments.

Experimental setup

The spectrally resolved fiber-photometry system in this study replicates an established system described previously[1]. Laser beams from a 488 nm 60 mW continuous wave (CW) laser (OBIS 488 LS-60, Coherent, Santa Clara, CA) and a 561 nm 50 mW CW laser (OBIS 561 LS-50, Coherent, Inc.) are aligned and

combined by broadband dielectric mirrors (BB1-E02, Thorlabs, Newton, NJ) and a long-pass dichroic mirror (ZT488rdc, Chroma Technology Corp), then launched into a fluorescence cube (DFM1, Thorlabs, Newton, NJ). Extra neutral density filters (NEK01, Thorlabs, Newton, NJ) are placed between the combined laser beam and the fluorescence cube to adjust the final laser power. The fluorescence cube contains a dichroic mirror (ZT488/561rpc, Chroma Technology Corp) to reflect and launch the combined laser beam through an achromatic fiber port (PAFA-X-4-A, Thorlabs, Newton, NJ) into the core of a 105/125 mm core/cladding multi-mode optical fiber patch cable. The distal end of the patch cable is connected to an implantable optical fiber probe for both excitation laser delivery and emission fluorescence collection. The emission fluorescence collected from the fiber travels back along the patch cable into the fluorescence cube, passes through the dichroic mirror and an emission filter (ZET488/561 m, Chroma Technology Corp, Bellows Falls, VT), then launches through an aspheric fiber port (PAF-SMA-11-A, Thorlabs, Newton, NJ) into the core of an AR-coated 200/230 mm core/cladding multi-mode patch cable (M200L02S-A, Thorlabs, Newton, NJ). The AR-coated multi-mode patch cable is connected to a spectrometer (QE Pro-FL, Ocean Optics, Largo, FL) for spectral data acquisition, which can be operated by a UI software OceanView (Ocean Optics, Largo, FL). In order to achieve concurrent recording during fMRI, trigger mode is used in OceanView, where the photometry system is synchronized with MRI using an Arduino micro-controller board.

The stimulation system uses a DAQ board (1208Hs-2AO, Measurement Computing Corp., Norton, MA) to send out stimulus triggers according to the stimulus paradigm set in a homemade software program. During fMRI experiments, the DAQ synchronizes stimulation pulses via triggers from the MRI system. Stimulation pulses were driven by a constant current stimulus isolator (A385RC, World Precision Instruments, Sarasota, FL) for forepaw and microelectrical stimulation experiments; and by a 473 nm blue diode laser (Shang Laser and Optics Century, BL473T8-200FC + ADR-800A, Shanghai, China) for optogenetic experiments.

Animal subject preparation and physiology management

Rats were initially anesthetized with 4% isoflurane (Vaporizer #911103, VetEquip Inc., Livermore, CA, USA) mixed with medical air and endotracheally intubated using a 14G x 2"(>400 g) or 16G x 2"(<400 g) i.v. catheter (Surflash Polyurethane Catheter, TERUMO, Somerset, NJ, USA). Respiration was maintained by a ventilator (SAR-830 or MRI-1, CWE Inc, Ardmore, PA, USA) set at 60 breaths/min and an inspiration time ratio of 40%. A rectal probe was used to monitor core body temperature (OAKTON Temp9500, Cole-Parmer, Vernon Hills, IL, USA) and a capnometer was used to monitor heart rate, peripheral blood oxygen saturation, and end-tidal CO_2 (SURGIVET® V90041LF, Smith Medical, Dublin, OH, USA). Body temperature was maintained at 37 ± 0.5°C using a circulating water blanket connected to a temperature adjustable water bath (Haake S13, Thermo Fisher Scientific, Waltham, MA, USA). Ventilation tidal volume was adjusted to keep the heart rate at 300 ± 50 beats per minute, peripheral blood oxygen saturation above 90%, and end-tidal CO_2 between 2.8 - 3.2%. End-tidal CO_2 values from this capnometer system were previously calibrated against invasive sampling of arterial blood gas, reflecting a partial pressure of carbon dioxide (pCO_2) level of 30–40 mm Hg[58,59]. For studies using Rhodamine B for CBV measurements, a bolus dose of 40 mg/kg (Sigma–Aldrich, St. Louis, MO) was injected via tail vein.

Concurrent functional MRI Scan with fiber-photometry recording

All fMRI data in this study were collected on a Bruker BioSpec 9.4-Tesla, 30 cm bore system with 6.0.1 on an AVANCE II console (Bruker BioSpin Corp., Billerica, MA). An RRI BFG 150/90 gradient insert (Resonance Research, Inc, Billerica, MA) paired with a Copley C700 gradient amplifier (Copley Controls Corp., Canton, MA) was used. A homemade single-loop surface coil with an internal diameter of 1.6 cm was used as a radio-frequency transceiver. Isoflurane concentrations were adjusted to 2% and animals were secured in to a custom-built, MR-compatible rat cradle. Animal physiology was monitored and maintained as described in the previous paragraph.

Upon stabilizing the animals, a pair of needle electrodes was inserted under the skin of forepaw for stimulation, or electrode/optical fiber patch cables were connected according to experimental design.

Before connecting the fiber-photometry patch cable, all light in the room was turned off, the final output power of 488 nm laser and 561 nm laser were adjusted to balance spectral amplitudes[1]. The maximum power used in this study was less than 100 μW. Then, a background spectrum was measured as a reference by pointing the fiber tip to a nonreflective background in the dark room. This background spectrum was then automatically subtracted by OceanView during photometry recording.

Following setup processes, the cradle was pushed into MRI bore, and a bolus of dexmedetomidine (0.025 mg/kg; Dexdormitor, Orion, Espoo, Finland) cocktailed with paralytic agent rocuronium bromide (4.5 mg/kg; Sigma–Aldrich, St. Louis, MO) was injected into the tail vein. Fifteen minutes after the bolus injection, continuous intravenous infusion of dexmedetomidine (0.05 mg/kg/h) and rocuronium bromide (9 mg/kg/h) cocktail was initiated and the isoflurane concentration was adjusted to 0.5–1% for the entire scanning period.

Magnetic field homogeneity was optimized first by global shim and followed by local first- and second-order shims according to B0 map. Anatomical images for referencing were acquired using a rapid acquisition with relaxation enhancement (RARE) sequence (12 coronal slices, thickness = 1 mm, repetition time (TR) = 2500 ms, echo time (TE) = 33 ms, matrix size = 256 × 256, field-of-view (FOV) = 25.6 × 25.6 mm^2, in plane resolution 0.1 x 0.1 mm, average = 8, RARE factor = 8). The center of the 5th slice from the anterior direction was aligned with the anterior commissure. Cerebral blood volume (CBV) fMRI scans were acquired using a multi-slice single-shot gradient echo echo-planar imaging sequence (GE-EPI) (slice thickness = 1 mm, TR = 1000 ms, TE = 8.1 ms, matrix size = 80 × 80, FOV = 25.6 × 25.6 mm^2, in plane resolution 0.32 x 0.32 mm, bandwidth = 250 kHz), with the same image slice geometry imported from the previously acquired T2-weighted anatomical image. A session of GE-EPI scans with 300 repetitions was taken, and at about the 100th scan, Feraheme (30 mg Fe/kg, i.v.) was administered for CBV percentage change calculations.

CBV fMRI Data Processing and Statistical Analyses

All fMRI data were analyzed using the Analysis of Functional Neuroimages (AFNI)[60] general linear model (GLM) framework[61]. All EPI images were skull-stripped, and slice-timing was corrected. Then automatic co-registration was applied to realign time-series data within subjects to correct subtle drift of EPI images. Finally all EPI images were aligned to a T2-weighted rat brain template[62] to generate normalized fMRI images to allow for group-level comparisons. Gaussian smooth (FWHM = 0.5 mm) was performed before feeding into the GLM fitting. To test the group-level significant consistency of the stimulus-evoked responses, we employed a parametric one-sample t-test implemented in AFNI. The false discovery rate correction was used to adjust for the multiple comparisons of fMRI maps ($p < 0.05$). A 3x3 voxel region of interest (ROI) was placed at the fiber tip in the S1 to extract fMRI time-course data. To account for Feraheme kinetics over the course of experiments, the following equations were used to calculate the $\Delta R_2^*(baseline)$, $\Delta R_2^*(stim)$, and ΔCBV [63].

$$\Delta R_2^*(baseline) = -\frac{1}{TE}\ln\left(\frac{S_{prestim}}{S_0}\right) \tag{22}$$

$$\Delta R_2^*(stim) = -\frac{1}{TE}\ln\left(\frac{S_{stim}}{S_{prestim}}\right) \tag{23}$$

$$\Delta CBV = \frac{\Delta R_2^*(stim)}{\Delta R_2^*(baseline)} \tag{24}$$

where $S_{prestim}$ and S_0 represents MR signal intensity after and before Feraheme injection, respectively, and S_{stim} are the MR signal intensities during the stimulation.

Fiber-photometry Spectral unmixing

Mixed spectra acquired by fiber-photometry were analyzed using a spectral linear unmixing algorithm[1]. Briefly, at any time point n, the mixed spectrum $Y(n)$ was modeled as:

$$Y(n) = Coff_1(n) \times S_1 + Coff_2(n) \times S_2 + C + \varepsilon(n) \tag{25}$$

where S_1 and S_2 are the normalized reference emission spectra of the two fluorescence signal sources. $Coff_1$ and $Coff_2$ are the unknown regression coefficients corresponding to the S_1 and S_2 respectively. C is

the unknown constant, and $\varepsilon(n)$ is random error. $Coff_1(n)$, $Coff_2(n)$, and $\varepsilon(n)$ at each time point were estimated using the lm() function in the RStudio package (RStudio Inc. V1.0.136, Boston, MA).

Modeling the hemodynamic response function

The relationship between neuronal activity and hemodynamic response can be expressed as:

$$HbT(T) = N(T) \otimes HRF(t) + c + d(T) \tag{26}$$

where the $HbT(T)$ represents hemoglobin fluctuation time-course, the $N(T)$ represents neuronal activity time-course, the $HRF(t)$ represents an impulse hemodynamic response function with t sampling points, c is a constant for baseline offset and $d(T)$ is for linear drift over time. Assuming $T = \{0, 1, 2, \dots, m\}$, $t = \{0, 1, 2, \dots, n\}$,this equation can be expressed as:

$$\begin{bmatrix} HbT(0) \\ HbT(1) \\ HbT(2) \\ \vdots \\ HbT(m) \end{bmatrix} = \begin{bmatrix} N(0) & 0 & 0 & & 0 & 1 & 0 \\ N(1) & N(0) & 0 & \cdots & 0 & 1 & \frac{1}{m} \\ N(2) & N(1) & N(0) & & 0 & 1 & \frac{2}{m} \\ & \vdots & & \ddots & & \vdots & \\ N(m) & N(m-1) & N(m-2) & \cdots & N(m-n) & 1 & 1 \end{bmatrix} \times \begin{bmatrix} HRF(0) \\ HRF(1) \\ HRF(2) \\ \vdots \\ HRF(n) \\ c \\ D \end{bmatrix} \tag{27}$$

Therefore, the $HRF(t)$, c and D (slope of $d(T)$) can be solved using Ordinary Least Squares solution with known $HbT(T)$ and $N(T)$.

To avoid physiological noise contamination, $HbT(T)$ were low-pass filtered with a cutoff frequency at 0.5 Hz before the HRF estimation.

Histology

At the end of the experiments, rats were euthanized by a mixture of 1-2 ml of sodium pentobarbital and phenytoin sodium (Euthasol, Virbac AH, Inc., Westlake, TX), and transcardially perfused with saline followed by 10% formalin. The brains were removed and stored in 10% formalin overnight, then transferred into a 30% sucrose solution (in 0.1 M phosphate buffer) for 2–3 days, until brains sunk to bottom of storage bottles. These brains were cut into serial coronal sections (40 μm) using a cryotome

(#HM450, Thermo Fisher Scientific, Waltham, MA) and mounted on glass slides. Fluoro-Gel II Mounting Medium (#17985-50, Electron Microscopy Sciences, Hatfield, PA) was covered on the brain slides to provide DAPI stain and for fluorescence imaging. Slides were imaged using a Zeiss LSM780 confocal microscope.

Extended Data Table 1: Average pathlengths $X(\lambda_{Ex})$ and $X(\lambda_{Em})$ by Monte Carlo Simulation.

Emission wavelength (nm)	Average $X(\lambda_{Ex})$ (cm)	Average $X(\lambda_{Em})$ (cm)
488	0.045093573	0.044381928
489	0.046031195	0.045206893
490	0.045353095	0.044599308
491	0.045145851	0.043833332
492	0.044940114	0.044644849
493	0.045780127	0.044951492
494	0.044833187	0.044238425
495	0.045254011	0.044087712
496	0.044832712	0.04357339
497	0.045793623	0.04438636
498	0.044556411	0.043741701
499	0.046485322	0.045282627
500	0.044936862	0.045399841
501	0.044904189	0.043737664
502	0.044676525	0.044692953
503	0.046449058	0.045104426
504	0.04554069	0.045690015
505	0.044186305	0.042754367
506	0.044463103	0.043549104
507	0.045240076	0.04375625
508	0.045271499	0.043551134
509	0.045203535	0.044181218
510	0.04544563	0.04325581
511	0.045264121	0.043061521
512	0.044537346	0.042787669
513	0.044684362	0.042203088
514	0.044171835	0.041233961
515	0.044738093	0.04226692
516	0.044465855	0.041780618
517	0.044712008	0.041028167
518	0.043706904	0.039055061
519	0.045479041	0.040324911
520	0.04389417	0.039274782
521	0.043549373	0.038231377
522	0.043219292	0.037524461
523	0.043155712	0.037460255
524	0.042766927	0.03694169
525	0.043084675	0.035815527
526	0.043150433	0.034397857
527	0.043739313	0.034308684
528	0.04204147	0.033144384
529	0.042283369	0.033431559
530	0.041576273	0.03274051
531	0.041403969	0.032249133
532	0.042259357	0.03207917

533	0.042053695	0.03107138
534	0.041557514	0.03060531
535	0.041085208	0.030560256
536	0.040797064	0.03006389
537	0.041257322	0.030668237
538	0.040610296	0.030040682
539	0.041278057	0.029169312
540	0.040911226	0.029855726
541	0.040595945	0.02918373
542	0.042377485	0.029198135
543	0.039844855	0.028926177
544	0.040222405	0.029041564
545	0.040557664	0.02896974
546	0.040948557	0.029918984
547	0.041229136	0.02972593
548	0.042018793	0.029700507
549	0.040926872	0.029586768
550	0.040638456	0.030291714
551	0.041457873	0.030528575
552	0.042017	0.030977213
553	0.041651907	0.03110746
554	0.041411748	0.031308639
555	0.043001153	0.031844072
556	0.041683419	0.031503805
557	0.041847941	0.031712862
558	0.042180993	0.031085786
559	0.042966746	0.031697395
560	0.041901694	0.032766419
561	0.041052921	0.032209208
562	0.042547549	0.032859811
563	0.043019746	0.031171994
564	0.042869082	0.031870075
565	0.04259555	0.031539041
566	0.042495922	0.031772912
567	0.041849738	0.03096196
568	0.042757629	0.031304522
569	0.042385588	0.031173599
570	0.040329248	0.029757283
571	0.041741617	0.029138568
572	0.041959	0.02928782
573	0.040394795	0.028463193
574	0.042377246	0.028834891
575	0.042868462	0.029326084
576	0.041217724	0.028643115
577	0.040870023	0.028252116
578	0.04152183	0.028335837
579	0.042072267	0.028919726
580	0.041743821	0.029298395

581	0.041806895	0.029681861
582	0.040685735	0.030320858
583	0.043016536	0.030965203
584	0.042402937	0.031996206
585	0.04392674	0.032806366
586	0.044501271	0.035278456
587	0.04229412	0.035422192
588	0.044236652	0.037092348
589	0.04453953	0.039432637
590	0.045403689	0.042120811
591	0.045720725	0.043050508
592	0.046721386	0.044569175
593	0.04658936	0.046035872
594	0.046856197	0.046439476
595	0.046639376	0.050515218
596	0.047224996	0.050214893
597	0.047826425	0.051104707
598	0.047684723	0.055223016
599	0.048337422	0.058213776
600	0.048084498	0.05737416
601	0.048056722	0.055091687
602	0.04834153	0.058816123
603	0.047162448	0.060133037
604	0.048829402	0.059604177
605	0.048451209	0.06028036
606	0.049314163	0.062367752
607	0.04864508	0.064056712
608	0.047748293	0.064284482
609	0.049373015	0.062747999
610	0.049654837	0.062923108
611	0.04873937	0.059863284
612	0.048195016	0.067000662
613	0.049368953	0.06636147
614	0.049471526	0.066356177
615	0.0509815	0.065962632
616	0.048364103	0.067198216
617	0.049258066	0.068526301
618	0.047925207	0.066248105
619	0.047651389	0.064842825
620	0.049918572	0.069186304
621	0.048079999	0.06930868
622	0.049001919	0.067431619
623	0.047876525	0.068410691
624	0.048913258	0.066037747
625	0.049283261	0.069188854
626	0.049833981	0.06884971
627	0.048520845	0.068593605
628	0.050626431	0.072924701

629	0.049001529	0.069368645
630	0.049823194	0.065875529
631	0.049922336	0.070392798
632	0.049238223	0.064130262
633	0.049091246	0.068703876
634	0.049004327	0.069478775
635	0.050113703	0.069644791
636	0.04935265	0.071714894
637	0.048524722	0.065578319
638	0.049033574	0.068908878
639	0.049706978	0.07082453
640	0.048870373	0.067637064
641	0.049378341	0.070513241
642	0.047531488	0.065338289
643	0.049938511	0.067545633
644	0.048420131	0.070092771
645	0.048394814	0.066225652
646	0.049045058	0.067036677
647	0.0471389	0.063334021
648	0.048276563	0.064587084
649	0.049566595	0.067005786
650	0.048757214	0.066615875
651	0.048086512	0.064861617
652	0.049770716	0.071548828
653	0.048497445	0.065184075
654	0.051019438	0.064323894
655	0.047818361	0.069356187
656	0.047395308	0.06791304
657	0.048211057	0.064465262
658	0.04925706	0.068522353
659	0.049243152	0.067570369
660	0.049306566	0.068635881
661	0.048296998	0.064357191
662	0.04946561	0.069889086
663	0.048651964	0.066769534
664	0.049580237	0.061861251
665	0.047312599	0.061431122
666	0.048177763	0.066106882
667	0.049260615	0.06726634
668	0.050070504	0.065101662
669	0.049296071	0.060405176
670	0.049355936	0.066502011
671	0.048166386	0.06328206
672	0.048552887	0.063599076
673	0.047215508	0.0630013
674	0.050010272	0.065692928
675	0.048251383	0.059550299
676	0.049073229	0.064339078

677	0.049158252	0.066160593
678	0.048586706	0.063461555
679	0.049408432	0.066435927
680	0.048615398	0.063448449
681	0.048136575	0.06465852
682	0.049240503	0.065996535
683	0.048443426	0.068781814
684	0.049338138	0.064378941
685	0.048442599	0.067303664
686	0.047661626	0.060606162
687	0.048758079	0.06567617
688	0.048292359	0.062784951
689	0.048590671	0.064714098
690	0.049590564	0.062694093
691	0.047962726	0.063263871
692	0.050139198	0.061484326
693	0.048513909	0.063766816
694	0.048005757	0.062790064
695	0.048824793	0.06817339
696	0.048301867	0.062689082
697	0.048157362	0.065482695
698	0.047640732	0.059392198
699	0.048021823	0.062982676
700	0.049106955	0.063966326

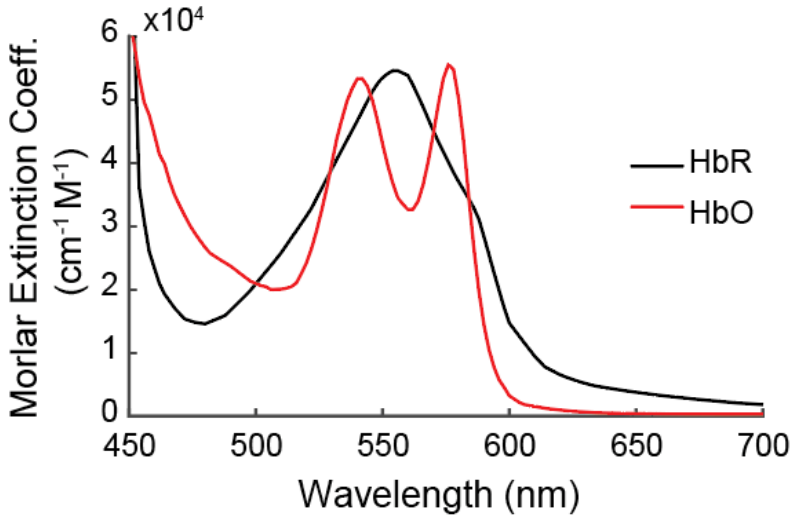

Extended Data Fig. 1 Molar extinction coefficients of HbO and HbR as a function of wavelength.

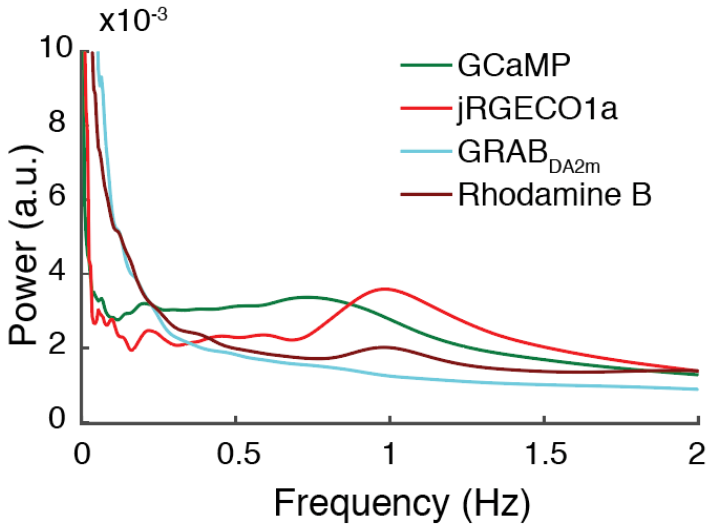

Extended Data Fig. 2. Power spectral distribution of several commonly used fluorescent sensors. Hemodynamic responses (CBV) were measured by intravenously injecting a long-circulating red fluorescent dye, Rhodamine B.

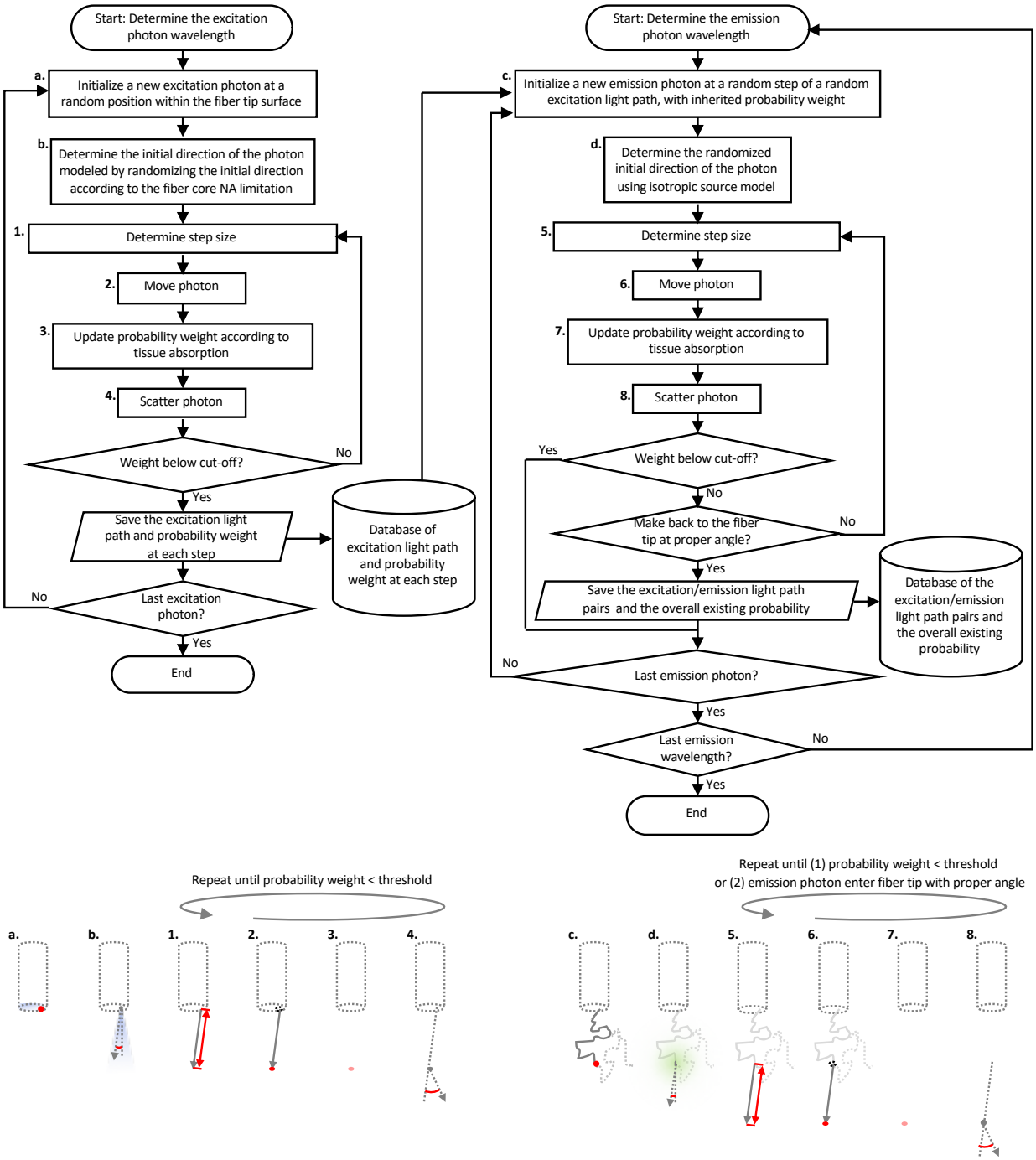

Extended Data Fig. 3. Light path simulation flow chart.

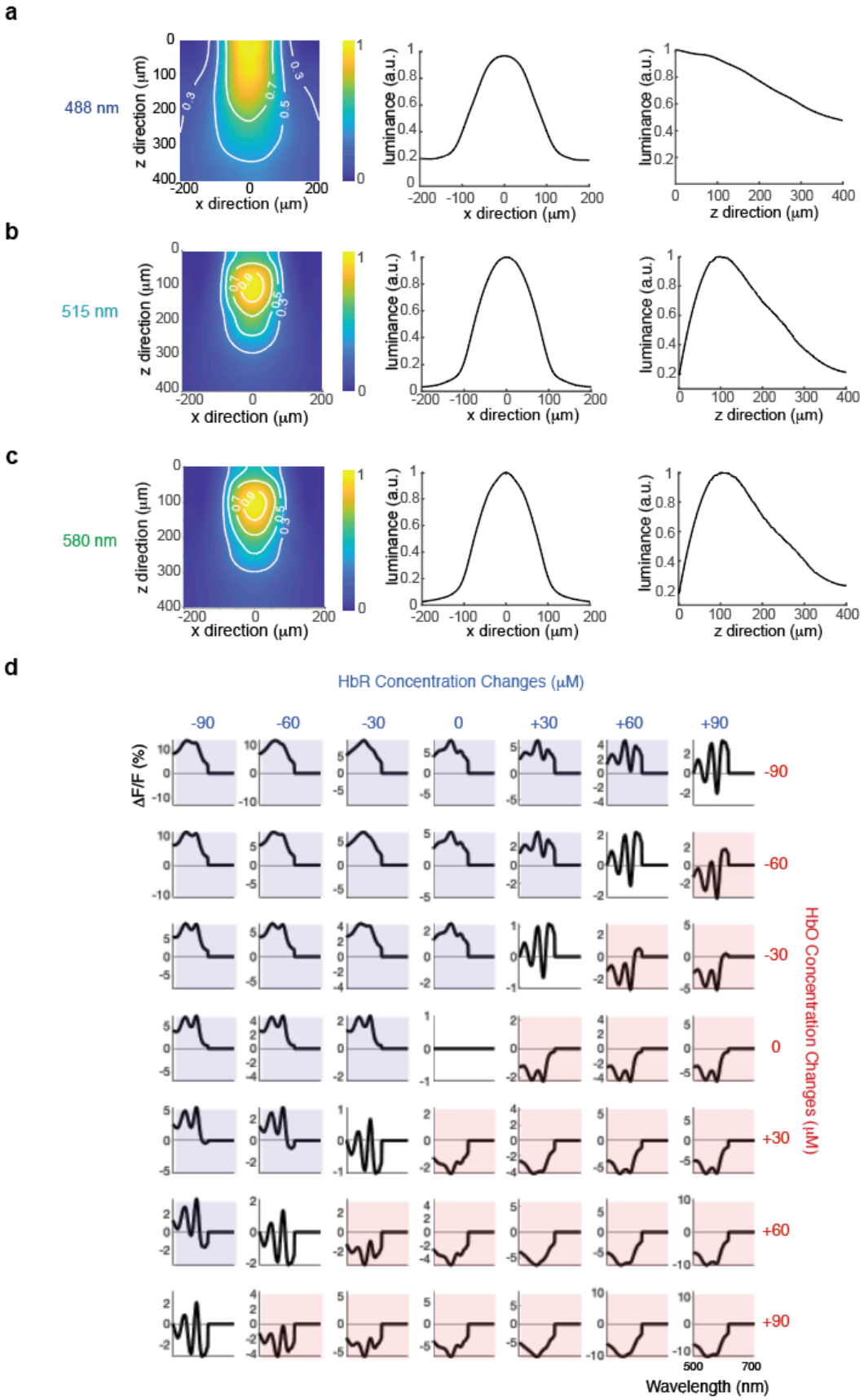
a
488 nm
515 nm
580 nm
z direction (μm)
x direction (μm)
luminance (a.u.)
z direction (μm)
b
c
d
HbR Concentration Changes (μM)
-90
-60
-30
0
+30
+60
+90
ΔF/F (%)
HbO Concentration Changes (μM)
Wavelength (nm)

Extended Data Fig. 4 Monte Carlo simulation results. Illuminating distribution of the excitation 488 nm light **(a)** and the receptive probability of two commonly used emission lights (515 nm and 580 nm, **b-c**). Left column showing the spatial probability maps, and middle and right columns showing normalized luminance-distance profiles in x and z directions. Color bar indicates probability from 0 to 1. **(d)** Simulated effects of HbO and HbR concentration changes on fluorescent signal measurement. ΔC_{Hb0} and ΔC_{HbR} ranging from -90 to +90 μM were used to simulate fluorescent signal changes (ΔF/F) between 500 to 700 nm using the molar extinction coefficients of HbO and HbR in **Extended Data Fig. 1** and simulated light paths in **Fig. 1c**. Graphs shaded in blue indicate an overall decrease in total Hb (HbT); whereas graphs shaded in red indicate an overall increase in HbT.

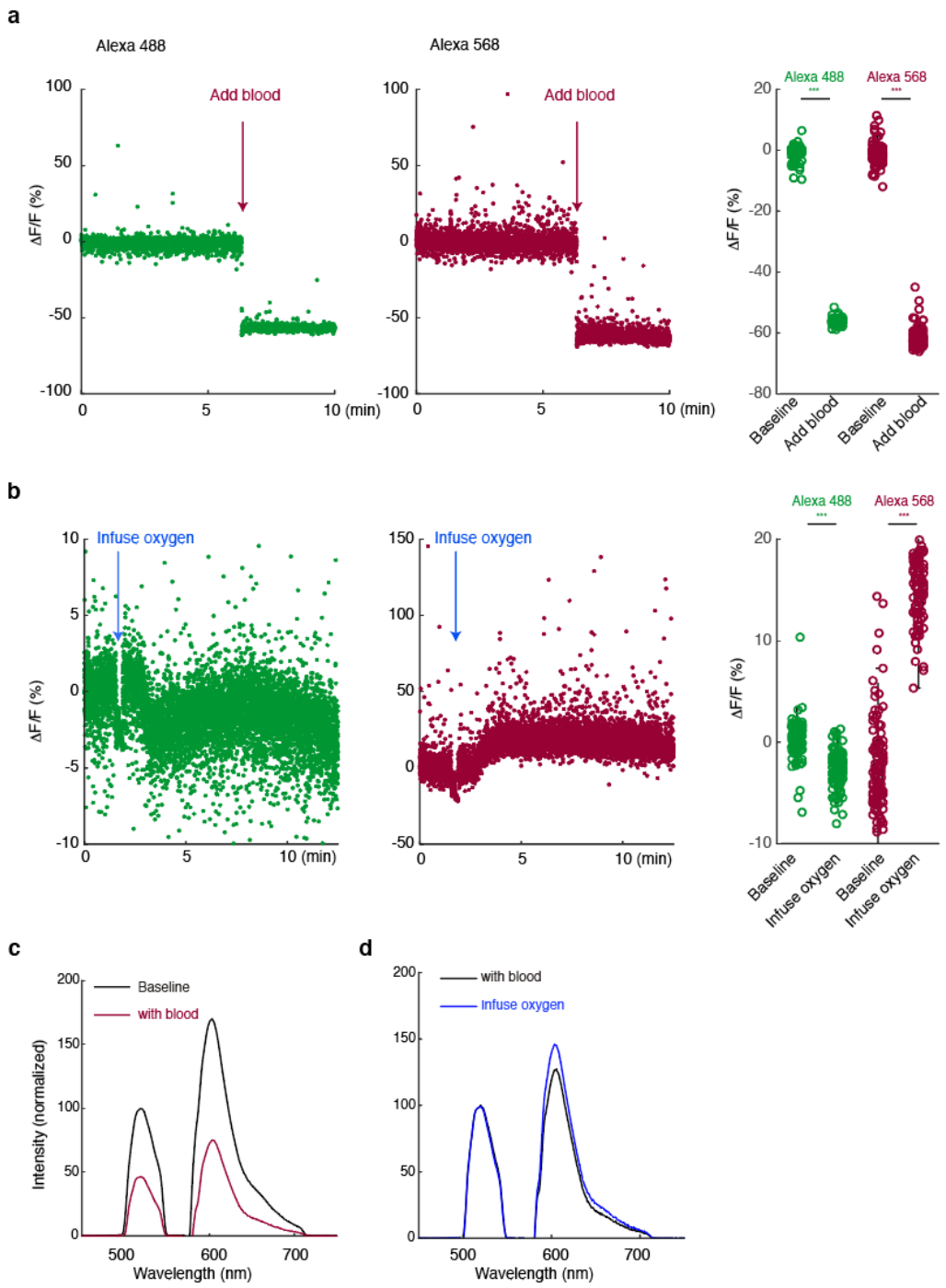

Extended Data Fig. 5. Ex vivo quantification of Hb-absorption effects on photometry recordings (**a**) ΔF/F changes before and after adding 1 mL of fresh mouse venous blood into 10 mL saline solution containing 10 μL Alexa 488 and 10 μL Alexa 568 fluorescent dyes. (**b**) ΔF/F changes before and after 100% oxygen infusion into the solution containing blood and fluorescent dye mixture. (**c**) Normalized intensity spectra of the fluorescent solution mixture before and after adding blood. (**d**) Normalized intensity spectra of the blood-fluorescent solution mixture before and after oxygen infusion. Error bars represent standard deviation. *** indicates $p < 0.001$ (*t*-test).

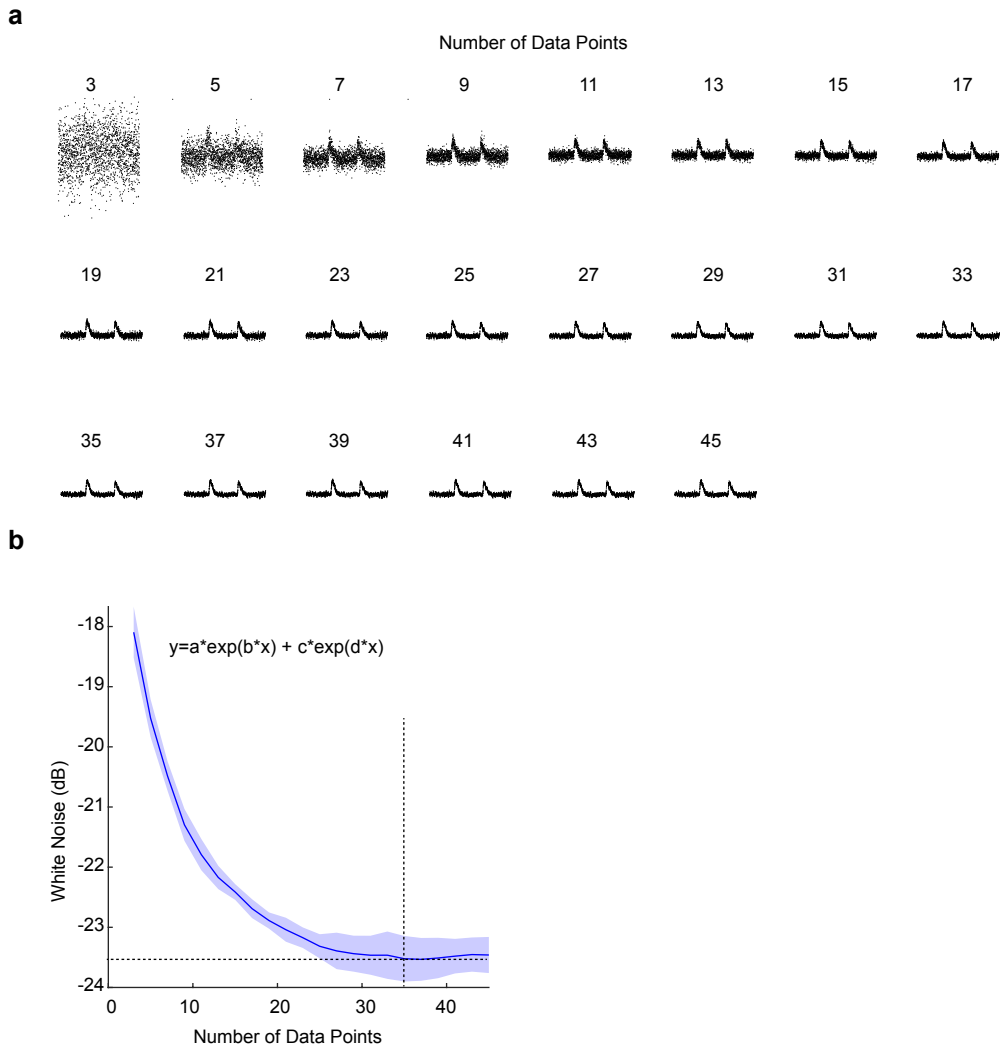

Extended Data Fig. 6. Number of spectral datapoints needed to derive reliable hemoglobin concentration changes. (**a**) Representative ΔC_{HbO} time courses derived from static EYFP data using different number of spectral datapoints ranging from 3 to 45 (centered at 523 nm). (**b**) Reduction of white noise was observed with increased number of datapoints. The derived ΔC_{HbO} exhibited minimized white noise when the number of datapoints reaching 35.

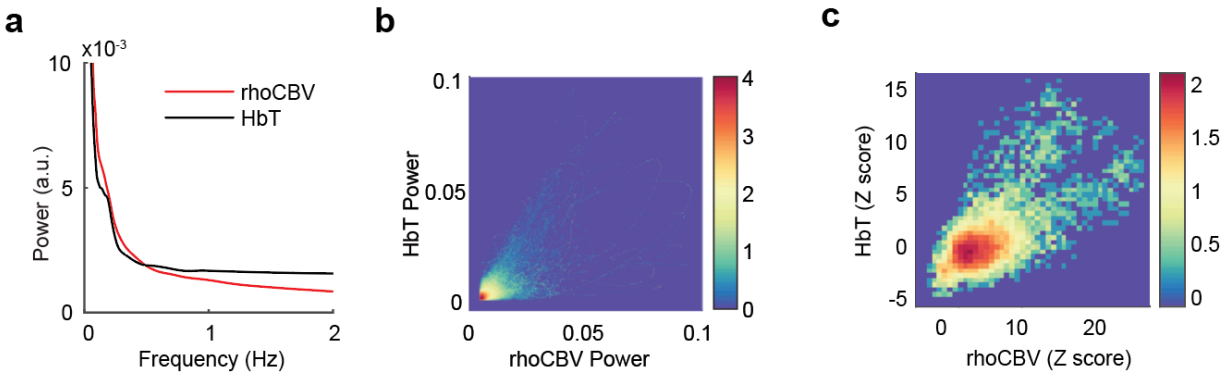

Extended Data Fig. 7. Comparison between corrected rhoCBV and HbT derived from EYFP signals. (**a**) Power spectral distribution. (**b**) Two-dimensional histogram summarizing rhoCBV and HbT power. (**c**) Two-dimensional histogram summarizing Z scores of rhoCBV and HbT. Colorbar indicates counts in log-scale.

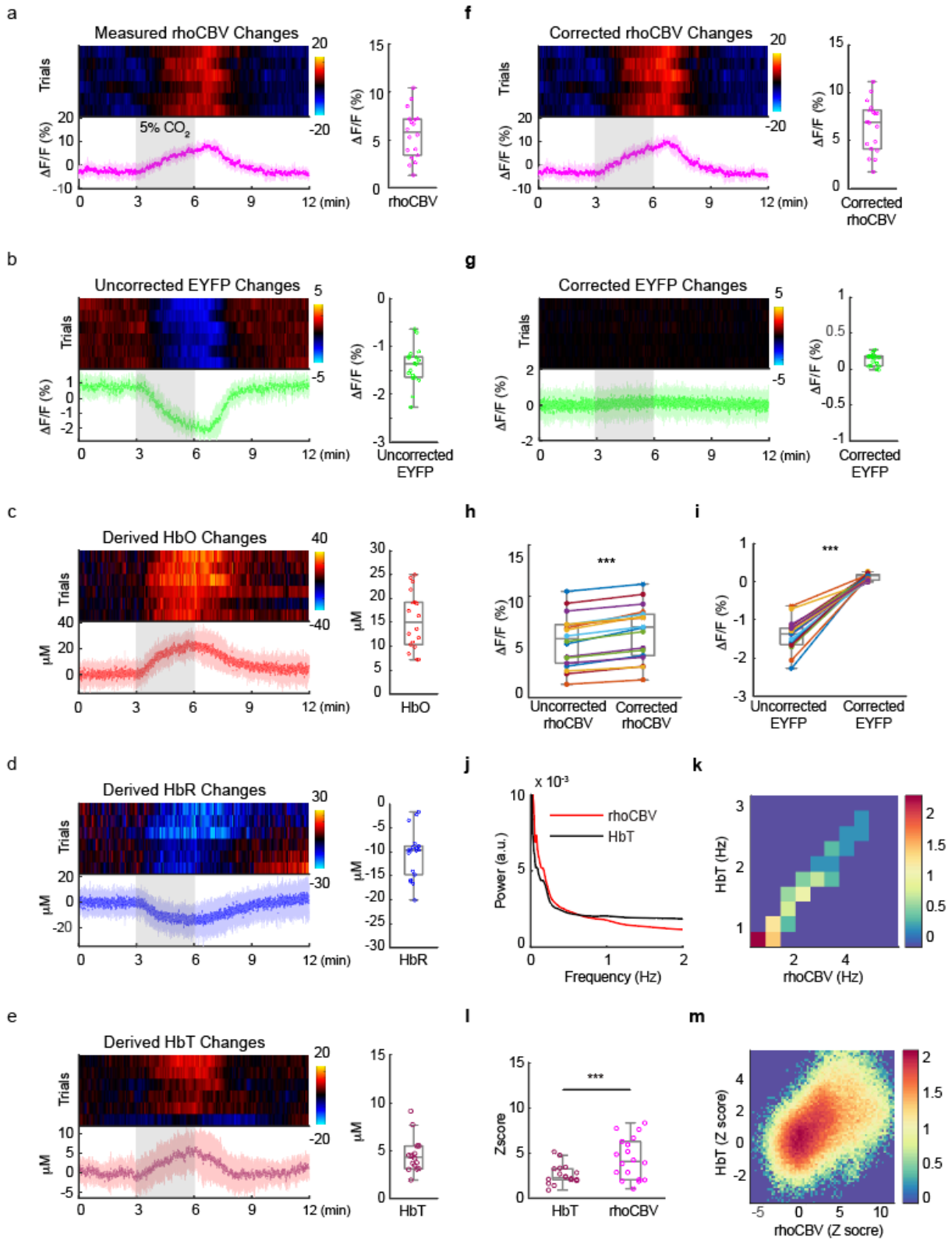

Extended Data Fig. 8: **Fiber-photometry in the S1 with EYFP during hypercapnia (5% CO_2).** (**a-g**) Peri-event heatmaps showing repeated trials and average response time-courses of the changes in measured

rhoCBV, measured EYFP, derived HbO, derived HbR, derived HbT, corrected rhoCBV, and corrected EYFP, respectively. The gray-shaded segment indicates infusion of 5% CO_2. All color bars use the same unit as the time-course Y axis. Error bars represent standard deviation. (**h,i**) Correction of the contaminated rhoCBV and EYFP signals, respectively, across all subjects and all trials (n=5, total trials =18; *** indicates $p < 0.001$, paired *t*-test). (**j**) Power spectral distribution. (**k**) Two-dimensional histogram summarizing rhoCBV and HbT power. (**l**) rhoCBV exhibited higher sensitivity than derived HbT. (**m**) Two-dimensional histogram summarizing rhoCBV and HbT Z scores. Colorbar indicates counts in log-scale. Error bars represent standard deviation. *** indicates $p < 0.001$ (paired *t*-test).

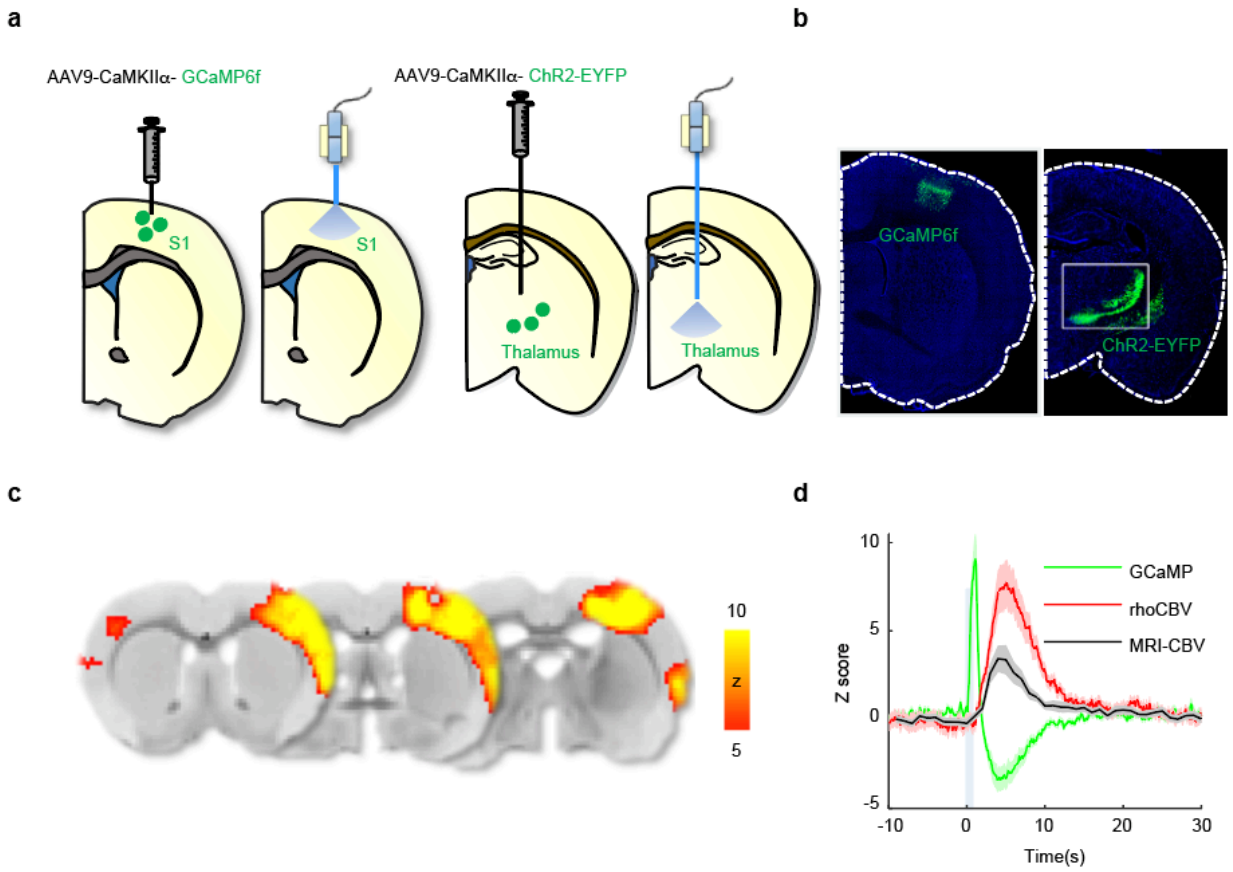

Extended Data Fig. 9. **Simultaneous fMRI and fiber-photometry recording showing optogenetic-evoked CBV-fMRI, GCaMP and rhoCBV changes in the S1.** (**a**) GCaMP and channelrhodopsin-2 (ChR2) were virally expressed using AAV under the CaMKIIα promoter in the S1 and ventroposterior (VP) thalamus, respectively. Rhodamine B was intravenously injected to achieve CBV measurement. (**b**) Confocal images showing GCaMP expression. (**c**) MRI-CBV activation maps in response to optogenetic stimulation of VP. (**d**) Uncorrected GCaMP, rhoCBV, and MRI-CBV time courses (n=3, total trials =33 trials). After a short optogenetic stimulation of VP (60Hz, 10mW power, 0.5 ms pulse width for 1 s), uncorrected GCaMP signal exhibited a strong undershoot with signal pattern mirrored the rhoCBV and MRI-CBV data, indicative of significant Hb absorption *in vivo*.

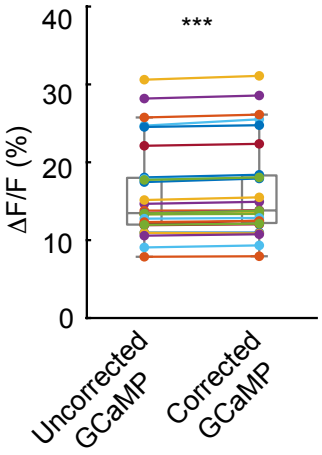

Extended Data Fig. 10. The peak amplitude of GCaMP responses is significantly higher in the corrected GCaMP compared with uncorrected GCaMP. (*** indicates $p<0.001$, paired *t*-test, n=27)

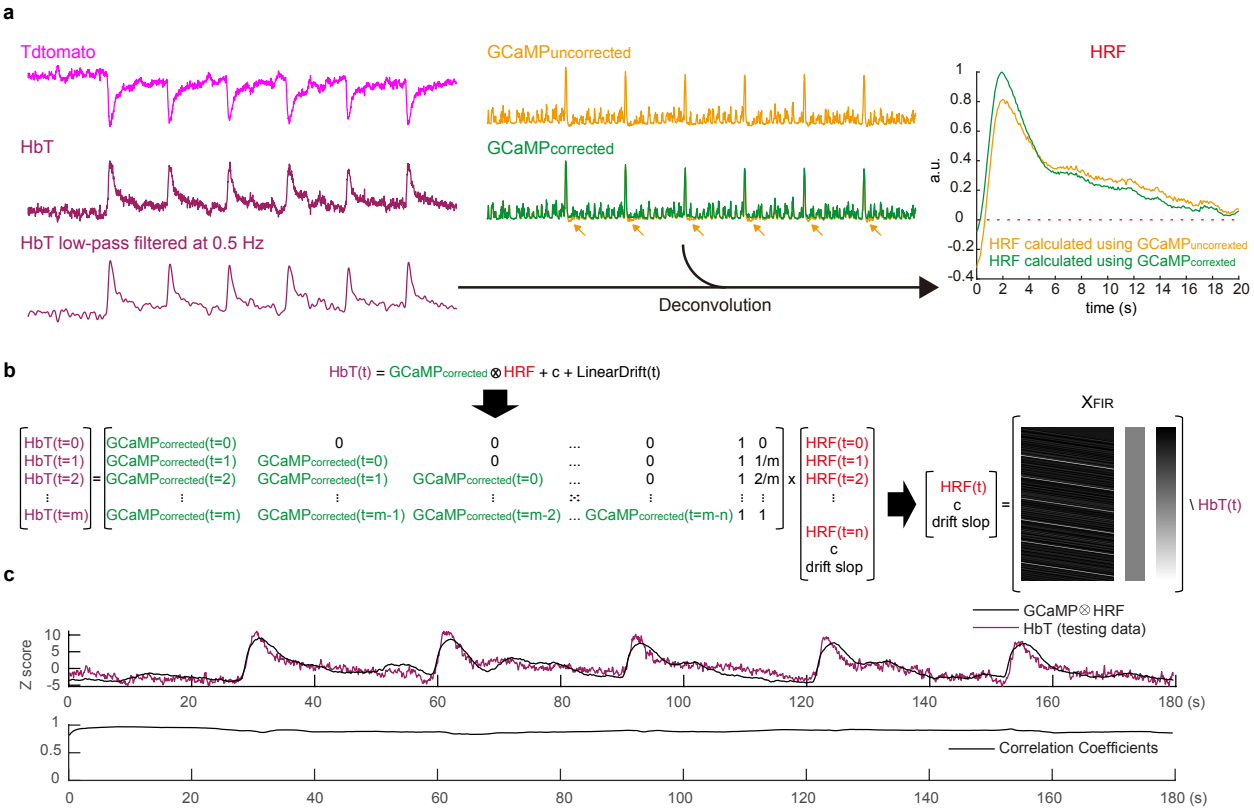

Extended Data Fig. 11. HRF calculation and validation. (**a**) Pipeline for estimating HRF from tdTomato-derived HbT and GCaMP signals. Yellow arrows indicate post-stimulus undershoot caused by Hb absorption. Using uncorrected GCaMP caused HRF intensity shift at t=0. (**b**) Strategy to deconvolve HRF form preprocessed HbT and GCaMP signals. (**c**) Validation of the HRF using a separate dataset naïve to HRF calculation. HRF was convolved with GCaMP data to predict HbT changes (black trace). High correlation was observed between the predicted and tdTomato-derived HbT (purple trace).

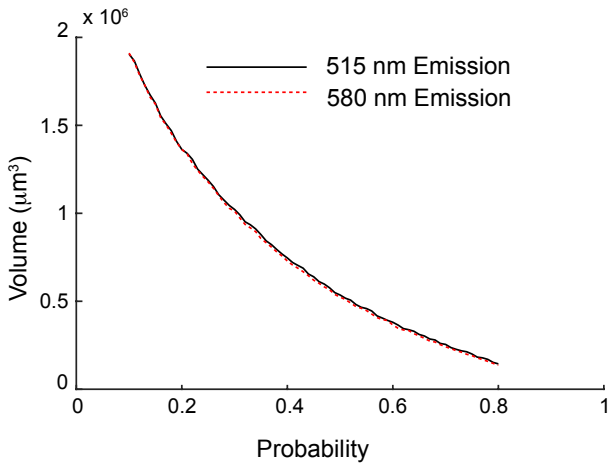

Extended Data Fig. 12. Simulated detection volume and its projected probability.

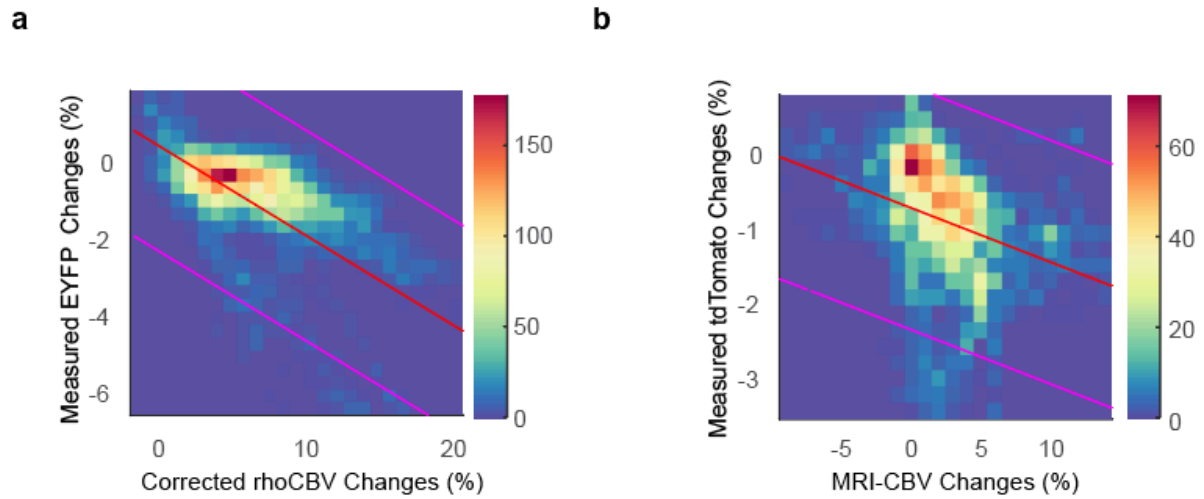

Extended Data Fig. 13. Signal drop in measured EYFP and tdTomato signals were correlated to the CBV changes. Color bars indicate counts.

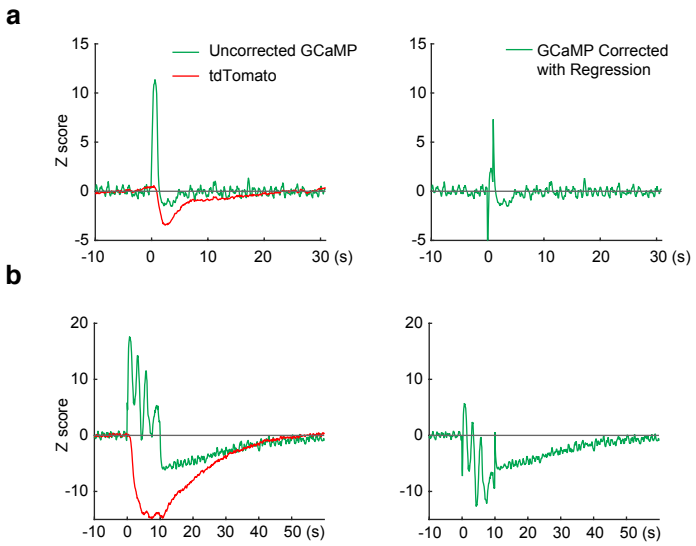

Extended Data Fig. 14. Correcting GCaMP signals by regression-out strategy (a) short (1 s), and **(b)** long (10 s) stimulations, respectively.

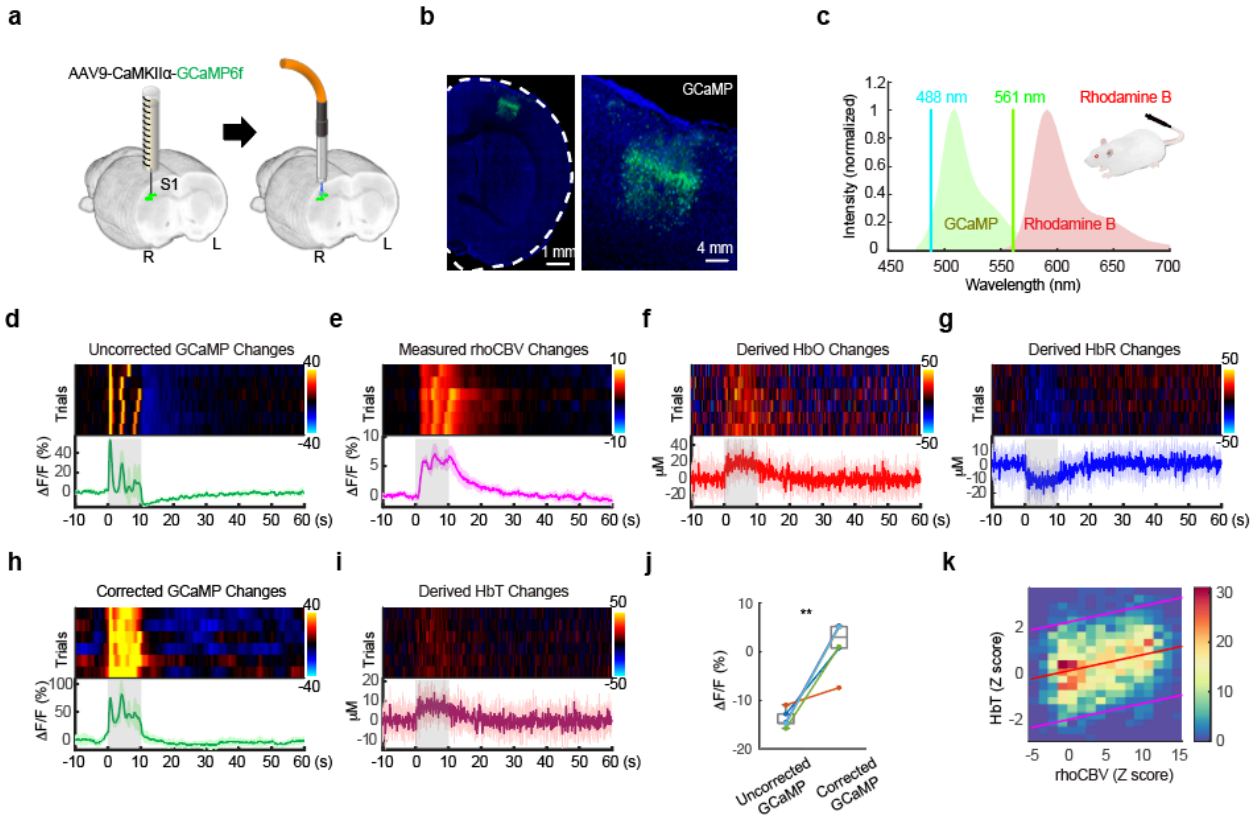

Extended Data Fig. 15. Quantification of Hb-absorption effects using residue signals of fiber-photometry

(**a**) Fiber-photometry measurement of GCaMP signal in the S1 of the forelimb region. (**b**) Confocal images showing GCaMP expression. (**c**) Simultaneous dual-spectral photometry recording of GCaMP and hemodynamic responses (CBV) was achieved by intravenously injecting a long-circulating red fluorescent dye, Rhodamine B. (**d-i**) Peri-stimulus heatmaps showing repeated trials and average response time-courses of the changes in uncorrected GCaMP, measured rhoCBV, derived HbO, derived HbR, corrected GCaMP, and derived HbT, respectively. The gray-shaded segment indicates forepaw-stimulation period. All color bars use the same unit as the time-course Y axis. Error bars represent standard deviation. (**j**) Correction of the post-stimulus dip of GCaMP signals (n = 2, total trials = 6; ** indicates $p < 0.01$, paired *t*-test). (**k**) Two-dimensional histogram summarizing rhoCBV and HbT Z scores. Colorbar indicates counts. Linear fit (red line) and 95% confidence interval (pink lines) are also shown.

Extended Video 1. One representative simulation of paired excitation and emission photons traveling. Left: Initial ballistic photon flow of a 488 nm excitation beam incident from the optical fiber. Right: Diffuse propagation of the elicited 561 nm emissions captured by the same fiber.